ABSTRACT

Title of thesis: RELATIVE NAVIGATION FOR
THE HUBBLE SERVICING MISSION
USING REFLECTED GPS SIGNALS

Ian Cohen
Master of Science, 2007

Thesis directed by: Professor Robert M. Sanner
Department of Aerospace Engineering

Autonomous rendezvous and docking is an important research area within the new exploration missions called forth by NASA. Relative navigation requires special sensors and algorithms to provide the necessary information. It may be possible to use reflected GPS signals as a source of "free" relative navigation measurements. Thus requiring no additional hardware except added algorithmic complexity. This thesis examines the use of an extended Kalman filter with reflected GPS measurements as a form of bi-static radar. It compares two different types of dynamic models, an absolute orbit model versus Hill's equations. The scenarios were implemented in Matlab using Satellite Toolkit to generate a high fidelity truth model. The thesis also examines visibility of reflected signals in a typical Hubble rendezvous scenario. This is done by approximating the Hubble as a cylinder, and using geometric optics to predict the reflective pattern.

RELATIVE NAVIGATION FOR HUBBLE SERVICING MISSION USING REFLECTED GPS SIGNALS

by

Ian Cohen

Thesis submitted to the Faculty of the Graduate School of the
University of Maryland, College Park in partial fulfillment
of the requirements for the degree of
Master of Science
2007

Advisory Committee:
Professor Dr. Robert M. Sanner, Advisor
Dr. John C Adams, Co-Advisor
Dr. Daryll Pines, Department Chair

Acknowledgements

To my advisor Dr. Robert Sanner: Thank you for sticking with me and supporting me throughout the last couple years. Especially all of those last minute corrections via email. Moreover, thank you for allowing me to pursue a particular topic more along my lines of interest and supporting me through the GPS portion. Even though it is not your particular field of expertise. Sorry for making you read such a long thesis!

To my co-advisor Dr. Carl Adams: Thank you for supporting me all these years, at NASA and academically. For helping me grow as a young aerospace engineer and mature into a Kalman Filter/GPS expert, and eventually a patent lawyer.

To my committee member Dr. Pines: Thank you for taking time out of your busy schedule to attend my defense and read my terribly long thesis.

To Dr. Bill Bamford: Thank you for helping/teaching me orbit dynamics, and common ways of debugging a Kalman filter.

To Vince Banes: Thank you for helping me out with some of the mathematics, radar equations, ad putting up with me through all these long weeks and all these tough questions! Also thank you for helping support my caffeine addition.

To Code 596, Miriam Wennersten, Greg Boegner, Chuck Clagget, Lamar Doughterty: Thank you for supporting me through the past couple years and particularly helping me further my educational goals and always giving me advice and guidance as a young engineer, and moreover as a young adult.

Table of Contents

List of Figures

List of Abbreviations

COTS	Commercial Off The Shelf
NASA	National Aeronautics and Space Administration
GPS	Global Positioning System
GSFC	Goddard Space Flight Center
SV	Space Vehicle
RMS	Root Mean Square
HST	Hubble Space Telescope
SM4	Servicing Mission 4
PRN	Pseudo-random noise
MULE	Multi-use Logistic Equipment Carrier
LHCP	Left Hand Circularly Polarized
LEO	Low Earth Orbit
RHCP	Right Hand Circularly Polarized
RF	Radio Frequency
RCS	Radar Cross Section
MSM	Mass Storage Module
SNR	Signal to Noise Ratio
STK	Satellite Toolkit

Chapter 1

Introduction

1.1 Motivation

All space programs wish to minimize risk. Part of this task includes automating the system in order to make it easier for manned missions, as well as unmanned missions to accomplish their tasks. This includes such tasks as rendezvous and docking, formation flying, and navigation. In recent years, there have even been several missions such as the ill-fated DART mission, Mars Express, and the Hubble robotic servicing mission, to test autonomous and rendezvous docking technologies. Specifically during the DART mission, there was an error causing the two satellites to collide. In order to reduce a risk of another such mishap, there is a need for extra measurements, and extra sensors capable of processing and handling the information to prevent other such mishaps from occuring and improve upon future technology.

Although it would be ideal to include the newest and best sensors, one of the viccs of space flight is to fly as cheaply as possible and as light as possible. Current relative ranging technologies such as LIDAR and camera pose algorithms are all extra technology and add complexity to the system and weight.

However, using existing technology, in this case a GPS receiver and a special antenna it is possible to extract information from the reflected signals and form a relative range solution. That is, without major hardware modifications, it is possible

to form a relative range solution with some added algorithmic complexity.

1.2 Previous Work

Although bi-static radar has not been applied specifically to the Hubble Rendezvous problem, it has been in use since the World War II era. There are many radar systems and papers based on using reflected signals to passively track and determine the position of aircraft, sea vessels, and spacecraft.

Hsu and Lorti present a brief overview of spaceborne bi-static radar architechture [6]. Another group from Italy, Moccia et. al, analyze the performance of a Spaceborne Sythetic Aperture Radar.[15]. Their paper evaluates the system performacne as a whole and addresses the problems and characteristics of a spaceborne SAR bi-static formation.

David Gaylor, Glenn Lightsey, and Kevin Key analyzed the effect of GPS multipath from the International Space Station. Their paper describes the multipath environment and signal blockage for a spacecraft operating in close proximity of the Space Station. In this situation the GPS multipath and lack of available signals can quickly degrade the performance of the GPS receiver and dilute their position solution. Their research was largely focused on modeling the multipath and signal blockage from the ISS[4]. From this model, David Gaylor and Glenn Lightsey went on to develop a GPS/INS Kalman filter for mitigating the multipath and signal blockage effects when operating in close vicinity to the ISS[5].

The application of tracking reflected GPS signals has also been focused on

ocean and land reflections. One of the interesting properties is using the reflected GPS signals to determine moisture content, sea roughness, wind speed and direction, and sea ice conditions.

Some previous work in tracking and acquiring reflected GPS signals was done by Dinesh Manandhar and Ryosuke Shibasaki at the University of Tokyo. Their research analyzed data from an LHCP/RHCP antenna pair to study the effect of multipath on a GPS signal. The multipath generated from a GPS signal consists of odd and even reflections. In theory odd reflections would be LHCP, while the even reflections would be RHCP[9].

Other researchers looking to exploit the GPS reflections also focus on land and ocean reflections. Currently, ocean reflections is a growing area of interest. David Masters et. al developed an algorithm for using GPS as a passive bistatic radar altimeter for aircraft navigation. There are SMEX, which are moisture experiments done using reflected GPS measurements.[11] They showed preliminary experimental results, and some expected performance from reflected signals[10]. Using an estimate model, they were able to get 0.68 m rms altitude error. Purely from the receiver's delay locked loop, they were able to get roughly a 2.5 m accuracy.

Relative satellite navigation has also been a heavy research area. W. Bamford presented his Ph.D. thesis on using GPS for establishing a network of satellites.[1]. GPS autonomous navigation itself has also been a busy research area, opening up many new opportunities for autonomous navigation.

Some other relative ranging strategies are using LIDAR and RADAR to actively range to a target. LIDAR can be extremely accurate, with accuracies on the

order of the wavelength of the laser, this can be sub-micrometer accuracy. Some of the drawbacks of LIDAR are that it requires extremely accurate pointing, and a generally higher power consumption.

The GRACE mission used a laser ranging system to accurately measure the distance between two spacecraft. This was done to measure the gravity field of the earth, which requires extremely high accuracies to detect the perturbations. The GRACE team was able to measure relative range to within $10\mu m$.[8] Johnson et. al looked into using LIDAR for Mars landing missions. It is able to get accuracies on the order of centimeters in their simulations.[7] Currently, the Space Shuttle uses a radar system for relative ranging and docking maneuvers. This provides an accurate relative range to within mm.[20]

The IRAS(intersatellite ranging and alarming system) is a GPS like active transmission scheme used to do relative range between spacecraft. It's transmitting a PN(psuedo-noise code) to do range determination. The phase for each space craft is aligned by phase, so the limiting factor is how accurately the phase can be determined. Current benchtop tests put the accuracy at less than 30m.

1.3 Outline of Thesis

The primary aim is to examine the relative nagivation problem applied to the specific Hubble rendezvous scenario and to develop a Kalman filter for relative navigation using the reflected GPS measurement.

Chapter 2 will describe an overview of the Global Positioning System. It will

describe the theory of oepration, the signal structure, and error sources. It will also discuss the measurements from the GPS constellation.

Chapter 3 begins with the generalized extended discrete Kalman filter. It will then apply the filter to a basic GPS navigation problem, then expand to the relative navigation problem applied to orbital dynamics. It will discuss the plant dynamics of the navigation problem and the linearizd measurement matrices for both a High Fidelity nonlinear model, and the linearized Hill's Model for relative spacecraft dynamcis.

Chapter 4 will provide an overview of the Relative Navigation Sensor(RNS) experiment. It will go into detail about the hardware and specifications of the GPS receiver.

Chapter 5 will discuss the simulated environment. It will begin with an overview of the rendezvous problem. It will also discuss the generation of the GPS constellation visibility and propagation. It will go into detail about the bi-static radar modeling and reflected signal visibility. It will conclude with a brief description of the generation of the pseudorange, pseudorange-rate, reflected psuedorange, and reflected pseudorange rate measurements for the simulated results.

Chapter 6 will address several different case studies and simulations performed in a Matlab environment. It will begin with a simple kalman filter scenario, building the orbital dynamics ontop of the basic model. Then reflective signal measurements will be included for relative ranging, and finally it conclude with the full scenario with the visibility mask.

Chapter 7 will address future work and provide a conclusion to the thesis.

Chapter 2

The Global Positioning System

2.1 Theory of Operation

This section provides a brief description of the GPS system as a whole. It will discuss the GPS system segments, a provide brief overview of the signal structure and theory.

2.1.1 Space Segment

The GPS space segment consists of the GPS constellation. The constellation nominally contains at least 24 satellites operating at any given time. There are six satellites in each of the 4 orbit planes at 55^o inclination. The nominal GPS Satellites parameters are listed below.

Orbit radius	26,561.75 km semimajor axis
Orbit Velocity(ECI)	$\sqrt{\frac{\mu}{r_{cs}}} = 3.8704$ km/s
ω_s Angular Velocity	$1.454x10^{-4}$ rad/s
Period	12 hr sidereal time
Inclination	55^o

Table 2.1: Approximate GPS Orbit Paramters

Each GPS satellite is equipped with an S-band communication link to the

ground, as well as the L-band GPS signal transmitters. One of the key features of the GPS constellation is its timing accuracy. Each satellite is equipped with either a cesium or rubidium atomic clock. This is vital for the frequency synthesizers on board which generate the L-band signals. The precision timing allows for accurate frequency and phase determination, enabling the system to generate very high positioning accuracies.

The two primary transmit frequencies are L_1 and L_2, at 1575.42 MHz and 1227.6 MHz respectively. This research is only concerned with the civilian L_1 signal.

2.1.2 User Segment

The GPS user segment consists of anyone who uses the GPS signals availible. This stretches from the military, to everyday users such as people with GPS car navigation devices. A very small, but steadily growing segment are the space users who take advantage of the GPS in orbit.

2.1.2.1 Space Usage

The space users consist of a very small portion of the overall user segment. The space user has to overcome several obstactles limited to the space environment. These include, but are not limited to, higher doppler rates, large dynamic ranges, extremely weak signals, and limited visibility.

2.1.3 Control Segment

The GPS control segment is the ground segment of the GPS System. This system keeps track of the GPS satellites health and ephemerides providing updates and corrections and housekeeping for them to maintain their orbits.

2.1.4 Signal Structure

The GPS L_1 signal is a CDMA signal broadcast at 1575.42 MHz. This signal is then spread by one of the unique satellite identifiers. Each satellite's identifier is known as a PRN code. This sequency is modulated onto the carrier by Binary Phase shift keying, inwhich each bit flip is a phase shift of 180 degrees. The spreading sequence has a chipping rate of 1.023 MHz, thus spreading the GPS signal over a 2 MHz bandwidth.

A data message is modulated on top of spread signal on at 50 bps. The data message contains information about the satellite's health, ephemeris, clock and tropospheric corrections, as well as information about the entire GPS constellation.

2.1.5 Basic Signal Acquisition and Tracking

The basic GPS measurement is the time of flight of the signal between the GPS Satellite and the user. In order to determine the time of flight, the receiver needs to be able to acquire and track the signal to determine its code phase with respect to the user.

The standard acquisition algorithm searches in serial through a grid of possible

time delays, Doppler shifts, and each possible PRN code. At each possible Doppler offset and code delay, known as a "Doppler bin", it generates a correlation. That is a correlation of the onboard replica code, with the GPS incoming signal. This correlation process can be thought of as a dot product in the time domain. This is in a sense, a matched filter lining up the code phase of the receiver's onboard code with the transmitted signal.

When the right Doppler bin is chosen, the signals line up in the code and carrier dimension, then the power is maximized. When the correlation passes a certain threshold, we declare that the signal is present, and hand off delay and doppler estimates to the tracking loops.

A typical tracking loop in a GPS reciever is the DLL loop. This operates by correlating the incoming signal against 3 different replica PRN signals generated onboard. Each of these signals is offset by -1/2 chip, 0 chips, and +1/2 chip and are referred to as early, prompt, and late respectively. This loop works by maximizing the prompt power and minimizing the early and late powers.

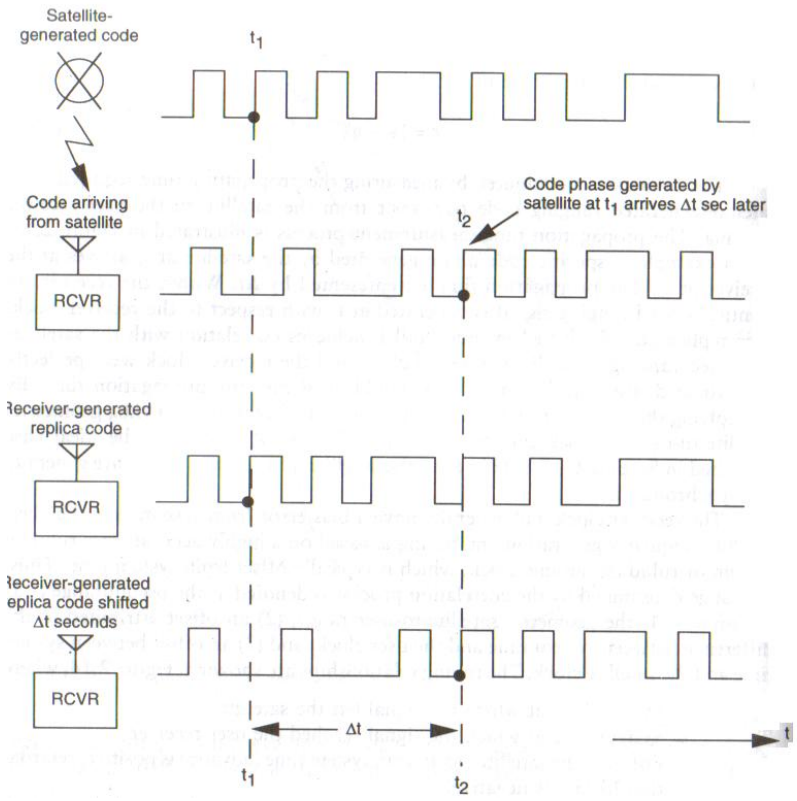

Figure 2.1: Replica Code Sync[14]

After the DLL has reached steady state, the locally generated PRN code phase is then synchronized with the incoming signal. After the code phase has synchronized, a typical GPS reciever drops into a phase-lock loop in order to lock onto the exact carrier phase within the doppler bin and wipeoff the data bits. This is done by tracking the exact phase of the signal, if it flips 180^o, then there is a databit transition.

The raw measurements come in the form of code phase, code rate, carrier phase, and carrier rate. These measurements directly relate to the pseudorange, and pseudorange rates.

In the case of the reflected signals, the incoming signal will be "smeared" in

the delay lock loop. This will effectively smear the correlation peak. Unfortunately, without emperical or measured performance, it is difficult to determine the shape of the reflected signal.

The satellite ephemerides are provided from the GPS data message. This provides us with an accurate position for each GPS satellite allowing us to solve for the line of sight vectors to each satellite and thus determine a position, velocity, and time solution.

2.2 GPS Measurements and Observables

The actual GPS measurements recorded from the constellation are the pseudorange and psuedorange rate. The pseudorange, ρ, is based on the time of flight between the GPS receiver and the GPS transmit antenna. This is used to form a range measurement, and thus solve for a position fix when enough satellites are availible. The other measurement availible is pseudorange rate, that is essentially the rate of change along the line of sight vector to the satellite. The psuedorage rate, $\dot{\rho}$, can also be viewed as the doppler shift on the signal. The pseudorange rate equation is equivalent to the carrier rate, $\dot{\Phi}$, which tends to be a less noisy measurement, however for the sake of simplicity, we'll use pseudo-range rate in our model.

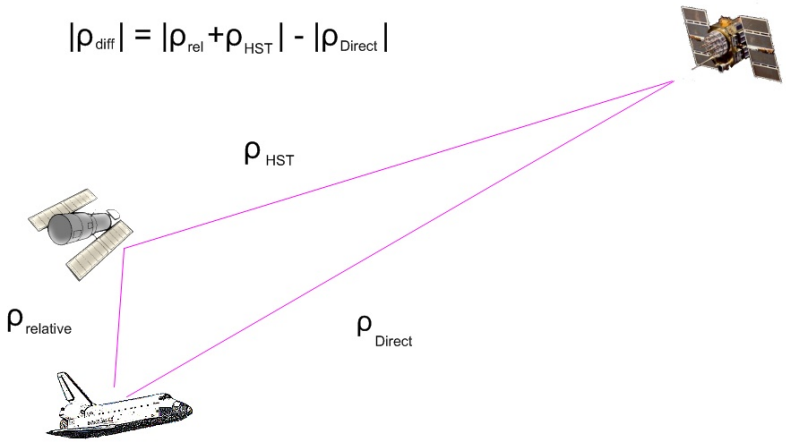

Figure 2.2: SatGeometry

The constructed measurements for the bistatic ranging problem are the differenced reflected psueodrange and the reflected psuedorange rate. The reflected psuedorange, ρ_R is differenced to remove some of the common mode errors allowing us to back out the relative position of Hubble. Some of the common mode errors removed are front-end jitter, receiver bias, thermal noise, and line bias. The psuedo range rate is the additive doppler shifts along the line of sight vectors between Hubble and the Shuttle, and between Hubble and the GPS constellation.

2.2.1 Pseudorange

The measured pseudorange is the difference between the system time at which the signal left the GPS satellite and the system time at which the signal reached

the user. This is given by

$$\rho = r + c(t_u + \delta t + \delta t_D) \tag{2.1}$$

r is the geometric range is given by $r = c(T_u - T_s)$, which is the exact time of flight between the user and the GPS satellite. t_u is the reciever offset from system time, δt is the offset of the satellite from system time, and δt_D is due to other measurement errors.

The GPS constellation is segmented into 3 parts, the user, the control, and space segment.

The 3 main sources for the space segment are satellite clock stability, clock perturbations, and selective availibility. For the control segment, it's primarily ephemeris prediction error. For the user segment it is ionospheric delay, multipath, reciever noise, and resolution.

The GPS satellite clock error is the residual error from a 2nd order polynomial fit, adjusting for relativsitic effects, the clock bias, clock drift, and frequency drift. The Satellite Clock error is on the order of 3.0 m.

The satellite ephemeris error is caused from the deviation in the current satellite ephemeride stored onboard the GPS satellite with the satellite's true position. These ephemeris values are used to form the line of sight vectors from each SV to the user, thus each perturbation adds error into the pseudorange. This is normally on the order of 4.2 m for a typical ground based GPS receiver.

The Department of Defense also implemented an option called Selective Availi-

bility, which is an intentional dithering of the ephemeris data to degrade the position solution. However, as of 1999, Selective Availibility is no longer in use by presidential edict.

The GPS system also experiences relativistic effects due to the gravitational potential differences.

Space users also experience ionospheric effects. This is generally seen as a bias in the measurement. The ionospheric effect is modeled off of the pathlength of the signal traveled through the ionosphere.

There are measurement errors from within the reciever. These are from the tracking loops internal to the GPS receiver. The dominant sources of error introduced here are the thermal noise jitter and dynamic stress error. The secondary sources are given by the hardware and software resolution, and clock drift.

The last source is multipath and shadowing effects. For the purposes of rendezvous, we are actually interested in tracking these multipath sources in order to solve for a relative position.

The GPS pseudorange error budget is on the order of 8.0 m for a standard GPS reciever located on the ground.

2.2.2 Pseudorange Rate

Pseudorange rate is a measurement of the rate of change of the psuedorange between the user and the GPS satellite. It is given by

$$\dot{\rho} = (V_u - V_g) \cdot \hat{los} + \epsilon \tag{2.2}$$

That is the rate of change of the psuedorange along the line of sight vector and the user. The error is mainly determined by the clock drift component. Generally these measurements are noisy compared to that of the pseudorange.

2.2.3 Differenced Reflected Psuedorange

This measurement is constructed from the difference in the direct path signal and the reflected signal. The equation is given by:

$$\rho_{\rho_r} = \rho_R - \rho_D \tag{2.3}$$

The measurements are differenced to remove some of the common mode errors of the measurement. After the differencing we are left with primarily the ionospheric effects, multipath, and thermal and tracking jitter.

Mathematically we arrive at:

$$\rho_{\rho_r} = r_{sh} + r_{hg} - r_{gs} + \epsilon \tag{2.4}$$

That is the sum of the geometric range from the Shuttle to Hubble, Hubble to the GPS satellite, and the Shuttle to the GPS satellite, plus the residual errors.

2.2.4 Reflected Pseudorange Rate

The psuedorange rate can be seen as a doppler shift on the signal. The reflection can be viewed as a retransmission, making it an additive process.

$$\dot{\rho_r} = (V_s - V_h)\hat{los_{sh}} + (V_h - V_g)\hat{los_{hg}} \tag{2.5}$$

Where the $\hat{los_{sh}}$ is the line of sight vector between the Shuttle and Hubble, and $\hat{los_{sh}}$ is the line of sight between Hubble and a GPS satellite. The primary sources of error contributing to the reflected psuedorange rate are the same of that as the direct measurement, however, the quality of the incoming signal is degraded due to the reflective process and the actual effect is unknown.

2.2.5 GPS Navigation Solutions

Typical GPS receivers use a simple least squares algorithm to determine position and time. It requires at least 4 visible satellites to solve for the four unknowns x,y,z, and the user clock offset from the GPS constellation. In addition to position estimates, some also do perform a finite difference of the positions to solve for velocity as well.

The first algorithms were able to provide around 30 meters of precision accuracy, however the newer GPS receivers can provide position solutions with under 5 meters of error, using differential GPS and other aiding techniques. These values are given with Selective Availability(SA) turned on. Since SA has been turned off, the error budgets have decreased to 10 meters and sub meter accuracy respectively.

In more advanced receivers, they sometimes implement a Kalman filter in order to utilize the dynamic information, as well as the measurements to improve the accuracy of the receiver. On orbit, the GPS receiver will experience large dynamic

stress and motion with respect to the GPS satellites, it is almost necessary to filter this heavily to provide a good navigation solution.

Chapter 3

The Kalman Filter

3.1 Introduction

The Kalman filter represents the optimal filter for a linear system with additive gaussian noise with zero mean. Since the dynamics of an orbiting body are well understood and their equations are well formulated, it is possible to exploit that information when forming the Kalman filter when applied to the relative navigation problem.

3.1.1 The Canonical Form of the Discrete Kalman Filter

The canonical form of the Kalman filter is given by [3]. It is the optimal filter for a linear system, incorporating a blending of the known dynamics, with that of the measurements. The discrete Kalman filter can be broken up into two distinct steps, the time update and measurement update.

The dynamical equations in a standard linear system are in the form:

$$\dot{X} = \mathbf{A}x + \mathbf{B}u + d \tag{3.1}$$

$$y = \mathbf{H}x + n \tag{3.2}$$

The catch is: These equations are *continous*. The equations need to be discretized in order to implement them in the Kalman filter.

This discretization is given by:

$$x_{k+1} = \mathbf{\Phi}_k x + \mathbf{\Gamma_k} u_k + d_k \tag{3.3}$$

$$y_k = \mathbf{H} x_k + n_k \tag{3.4}$$

$$\tag{3.5}$$

This relates timestep k-1, to timestep k. In order to calculate the state evolution between timesteps, for a linear system, the state transition matrix Φ is given by:

$$\mathbf{\Phi}_k = e^{\mathbf{A}\Delta T} \tag{3.6}$$

Where $\Delta T = t_{k+1} - t_k$.

The evolution of $\mathbf{\Gamma}$ is a bit more complex, it is given by:

$$\mathbf{\Gamma}_k = \int_0^T e^{\mathbf{A}\Delta\tau} \mathbf{B} u(\tau) d\tau \tag{3.7}$$

This model only concerns the unforced dynamics, so without loss of generality, $\mathbf{B}$ is assigned 0 and $\mathbf{\Gamma}$ is dropped. Now these equations can be applied to the Kalman filter form.

3.1.1.1 Time Update

The first step in the Kalman filter is to propagate the measurement from time-step k to the time-step k+1. This is done by multiplying by the state transition matrix, or integrating from t_k to t_{k+1}.

$$\hat{x}_{k+1}^{-} = \mathbf{\Phi_k}\hat{x}_k + \mathbf{\Gamma}_k u_k \tag{3.8}$$

Now to propagate the error covariance matrix.

$\mathbf{P}$ is defined as $\mathbf{P} = E\left[(\hat{x} - x)(\hat{x} - x)^T\right]$[3], it represents the variance in the estimator errors.

The error covariance propagation step is given as follows[3]:

$$\mathbf{P}_{k+1}^{-} = \mathbf{\Phi}_k \mathbf{P}_k \mathbf{\Phi}_k^T + \mathbf{Q} \tag{3.9}$$

3.1.1.2 Measurement Update

The first step of the measurement update is to form the Kalman Gain, $\mathbf{K}_k$. The Kalman gain is the optimal estimate to minimize the errors along the diagonal of the covariance matrix.[3]

$$\mathbf{K}_k = \mathbf{P}_k^{-}\mathbf{H}_k^T(\mathbf{H}_k\mathbf{P}_k^{-}\mathbf{H}_k^T + \mathbf{R})^{-1} \tag{3.10}$$

The next step is to apply the gain to the measurement error. The H matrix is the measurement connection matrix, it connects the states with the measurement at time-step k.

$$\hat{x}_k = \hat{x}_k^{-} + \mathbf{K}_k(z_k - \mathbf{H}_k\hat{x}_k^{-}) \tag{3.11}$$

The final step is to correct the error covariance for time-step k.[3]

$$\mathbf{P}_k = (\mathbf{I} - \mathbf{K}_k\mathbf{H})\mathbf{P}_k^- \tag{3.12}$$

3.1.2 The Extended Kalman Filter

While the equations are relatively straight forward in the discrete Kalman filter, they require one thing: The measurement model, and the plant dynamics are both linear systems. Unfortunately, in the real world most systems are nonlinear in nature and even worse for the GPS scenario there is also a non-linear measurement model.

The solution to a nonlinear measurement model can be done by approximating y_k. Given a nonlinear measurement model $y = h(x)$

$$y_k = \mathbf{H}_k x_k \tag{3.13}$$

$$\mathbf{H}_k = \left.\frac{\partial h}{\partial x}\right|_{\hat{x}_k} \tag{3.14}$$

3.2 The Basic GPS Navigation Problem

Let us first apply this filter to the basic GPS Navigation problem, similar to the one found in a typical car navigation system. The first step is to define a state vector, $x = [r, v, \delta t]^T$. These are positions, velocities , and time bias respectively.

For a simple first order system:

$$\dot{r} = v + d_n \tag{3.15}$$

$$\dot{v} = 0 + d_v \tag{3.16}$$

$$\dot{\delta t} = 0 + d_t \tag{3.17}$$

The time rate of change of velocity is set to 0, because it is impossible to predict the acceleration or motion of a vehicle. d_r, and d_v represent the modeling error of the dynamic equations.

3.2.1 State Transition Matrix

Now to form the state transition matrix equations, the dynamic equations are simply the discretized motion from time steps, n to n+1.

The state transition equations are given by:

$$r_{n+1} = r_n + v_n \Delta T$$

$$v_{n+1} = v_n$$

$$\delta t_{n+1} = \delta t_n$$

This holds for small velocity perturbations over a short time interval. Equivalently, this can written this as

$$\mathbf{\Phi}_k(t_1, t_0) = \begin{bmatrix} \mathbf{1}_{3x3} & \mathbf{1}_{3x3}\Delta T & \mathbf{0}_{3x1} \\ \mathbf{0}_{3x3} & \mathbf{1}_{3x3} & \mathbf{0}_{3x1} \\ \mathbf{0}_{1x3} & \mathbf{0}_{1x3} & 1 \end{bmatrix} \tag{3.18}$$

3.2.2 Measurement Equation

The measurement equation is needed to connect the states to the measurements, for GPS the is the pseudorange. This is given by :

$$\rho = r + c(t_u + \delta t + \delta t_D) \tag{3.19}$$

Taking this as the measurement, $h(x) = \rho = r + c(t_u)$.

$$\begin{aligned} r_x &= x_g - x_u \\ r_y &= y_g - y_u \\ r_a &= z_g - z_u \end{aligned} \tag{3.20}$$

where g is the g'th gps satellite from the users position, and u represents the user. Now to form the estimated pseudorange.

$$\rho = r + c(t_u) \tag{3.21}$$

In order to form the Kalman gain, it is necessary to linearize the measurement equations with respect to the state vector.

$$H_\rho(x) = \frac{\partial h(x)}{\partial x} \tag{3.22}$$

In this case it is simply the line of sight vectors to the user, along each axis. The time bias is a constant, which simply resolves to 1.

$$H_\rho(x) = \begin{bmatrix} \frac{r_x}{r} & \frac{r_y}{r} & \frac{r_z}{r} & 0 & 0 & 0 & 1 \end{bmatrix} \tag{3.23}$$

Now for the velocity corrections, the pseudorange rate provides the measurements. The measurement equation for pseudorange rate is given as follows:

$$h_{\dot{\rho}}(x) = \dot{\rho} = (v_g - v_u)_x los_x + (v_g - v_u)_y los_y + (v_g - v_u)_z los_z \tag{3.24}$$

The los vectors are given by $\frac{x_g - x_u}{r}$, they are the unit vectors pointing to the GPS satellite.

Taking partials with respect to the state vector:

$$H_{\dot{\rho}}(x) = \begin{bmatrix} (v_g - v_u)_x(\frac{1}{r} - \frac{(x_g - x_u)^2}{r^3}) \\ (v_g - v_u)_y(\frac{1}{r} - \frac{(y_g - y_u)^2}{r^3}) \\ (v_g - v_u)_z(\frac{1}{r} - \frac{(z_g - z_u)^2}{r^3}) \\ los_x \\ los_y \\ los_z \end{bmatrix}^T \tag{3.25}$$

Now that all the components to the measurement vector, $\mathbf{H}(x)$ have been defined. Thus connecting each of the measurements to the observables, pseudorange and pseudorange rate, it is necessary to define the measurement covariance matrix.

Now stacking the measurements, gives

$$\mathbf{H}(x) = \begin{bmatrix} \mathbf{H}_{\rho}(x)_n \\ \mathbf{H}_{\dot{\rho}}(x)_n \end{bmatrix} \tag{3.26}$$

Where n is the number of measurements. The measurement at timestep k is given by:

$$\mathbf{H}_k = \mathbf{H}(x)|_{\hat{x}_k} \tag{3.27}$$

3.2.3 Covariance Matrices

Now the last part needed for the Kalman filter are the measurement covariance, and process noise matricies, $\mathbf{R}$, and $\mathbf{Q}$ respectively.

The measurement covariance matrix consists of the variance of noise on the signal. From the canonical form: $y_k = \mathbf{H}_k x_k + n_k$, it can be shown that $\mathbf{R} = E\left[n_k n_k^T\right]$

Assuming uncorrelated gaussian white noise with zero mean, R is given by:

$$\mathbf{R} = \begin{bmatrix} \sigma_\rho^2 \mathbf{I}_{nxn} & \mathbf{0}_{nxn} \\ \mathbf{0}_{nxn} & \sigma_{\dot{\rho}}^2 \mathbf{I}_{nxn} \end{bmatrix} \tag{3.28}$$

The process noise matrix is given by the variance unmodeled forces in the dynamic model. Assuming we have a model: $x_k = \mathbf{\Phi}_k x_k + \mathbf{\Gamma}_k u_k + d_k$, noise actually enters the system as a disturbance on the input.

$$\mathbf{Q} = \mathbf{\Gamma}_k E\left[d_k d_k^T\right] \mathbf{\Gamma}_k^T \tag{3.29}$$

Unfortunately, the equation to describe the matrix $\mathbf{Q}$ is difficult to obtain because it requires calculation of $\mathbf{\Gamma}$. In the simulations, $\mathbf{Q}$ is treated as a free variable, adjusting it to give the optimal performance, and reduce the process covariance bounds such that they were roughly equal to the measured variance in $\mathbf{R}$.

This is given by:

$$\mathbf{Q} = \begin{bmatrix} \sigma_v^2 \Delta T^4 \mathbf{I}_{3x3} & \sigma_v^2 \Delta T^3 \mathbf{I}_{3x3} & \mathbf{0}_{3x1} \\ \sigma_v^2 \Delta T^3 \mathbf{I}_{3x3} & \sigma_v^2 \Delta T^2 \mathbf{I}_{nxn} & \mathbf{0}_{3x1} \\ \mathbf{0}_{1x3} & \mathbf{0}_{1x3} & \sigma_b^2 \end{bmatrix} \tag{3.30}$$

This filter performs well for ground based GPS receivers, particularly those

undergoing simple motion. However, in space, the relative velocities are extrememly large and the linearized dynamic equations begin to break down.

Since we have added knowledge about the particular dynamics of the system, we can incorporate this into an enchanced Kalman filter coupling the GPS measurements with our orbital dynamics.

In the case of relative navigation, it is a necessity to be able to approximate your relative position as well as possible. One of the best ways, is to have an accurate dynamic model. That way, you can rely on the dynamic model to propagate through measurement outages and noisy measurements. This is especially true in the case of applying reflected GPS measurements.

3.3 Relative Navigation Kalman Filters

The necessary components needed to construct our filter must be defined in order to begin formulating our Kalman filters for the relative navigation problem.

Given a dynamical system:

$$\dot{x} = f(x) \tag{3.31}$$

$$y = h(x) \tag{3.32}$$

$$\tag{3.33}$$

In order to begin the Kalman filter formulation, it is first necessary to define a state vector, X.

3.4 State Vectors

Let us begin by defining the states used in an absolute model, these are the absolute positions and velocities of the Shuttle and HST, as well as the bias state for the navigation solution. Typically a GPS receiver would include the bias drift as another component. For this simulation, since the rendezvous is over a short period of time, bias drift is neglected.

$$x = [r_s, v_s, r_h, v_h, b]^T \tag{3.34}$$

For a completely relative model Hill's equations are used to propagate the states. This requires formulating the problem entirely in a relative frame. The states in this case are

$$X = [\Delta_r, \Delta_v]^T \tag{3.35}$$

In this formulation, Δ_r is the relative position in hill's frame and Δ_v is the velocity.

3.5 Dynamic Model

Typically the dynamic model is a nonlinear equation given by a $\dot{x} = f(x)$. In this analysis two different model are examined. The first model model is based purely on the 2 body equation of motion given by Hill's equations. This model is a linearized representation of the relative spacecraft dynamics and has the form $\dot{x} = \mathbf{A}x$. Where $\mathbf{A}$ is given by the partials of $f(x)$ evaluated along a reference

trajectory.

$$\mathbf{A} = \left.\frac{\partial f}{\partial x}\right|_{\hat{x}_k} \tag{3.36}$$

The second model is a nonlinear higher fidelity model encompassing the J2 correction, and atmospheric drag.

3.5.1 Hill's Model

Hill's model is conveniently linear, simplifying the application of the Kalman filter. Hill's model is only valid for close proximity manevuers. Hill's model also requires a special coordinate frame to operate in, centered on a circular orbit for one of the vehicles.

3.5.1.1 Coordinate Frame

Hill's equations of motion are derived in the $\hat{R}, \hat{S}, \hat{W}$ coordinate frame. $\hat{R}$ is the radial direction from the center of the earth, $\hat{S}$ is the projection of the velocity in the plane perpendicular to $\hat{R}$, and $\hat{W}$ is the direction of angular momentum perpendicular to the orbital plane.

The transformations from the IJK coordinate frame are as follows:

$$\hat{R} = \frac{R}{|R|} \tag{3.37}$$

$$\hat{S} = \hat{W} \times \hat{R} \tag{3.38}$$

$$\hat{W} = \frac{\hat{R} \times \dot{\hat{R}}}{|\hat{R} \times \dot{\hat{R}}|} \tag{3.39}$$

Where r and $\dot{r}$ are the position and velocity vectors in the IJK reference frame.

Since Hill's frame is a relative frame, typically one spacecraft is chosen to be the reference orbit. This orbit is ideally circular. In this case, the orbit chosen is the space shuttle. This is denoted by r_{tgt}, the other spacecraft is typically called the interceptor or r_{int}.

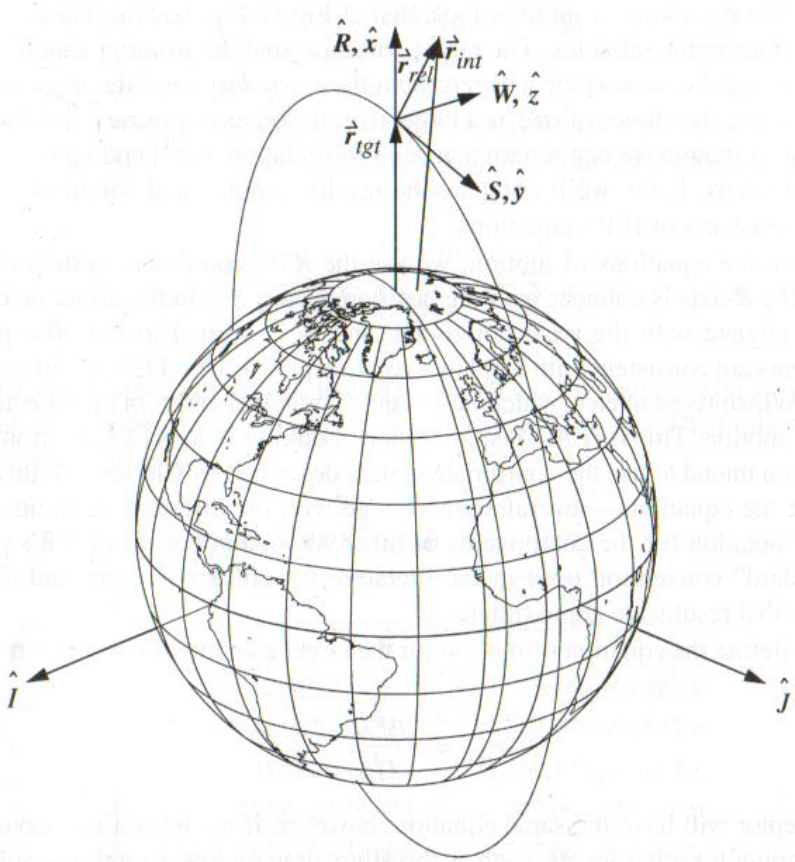

Figure 3.1: Hill's Coordinate Frame[21]

3.5.1.2 Dynamic Model

Hill's equations, also known as the Clohessy Wiltshire equations are the governing forces for relative two-body motion. These equations are well studied and even have an explicit solution. The derivation of Hill's equations are given in Appendix A.

$$\ddot{x} - 2\omega\dot{y} - 3\omega^2 x + fx = 0 \tag{3.40}$$

$$\ddot{y} + 2\omega\dot{x} + fy = 0 \tag{3.41}$$

$$\ddot{z} + \omega^2 z + fz = 0 \tag{3.42}$$

or, by defining $x^T = (x, \dot{x})$, then provides the form $\dot{x} = f(x)$. Now, taking partials with respect to the states, arriving at the canonical linear system form $\dot{x} = \mathbf{A}x$.

$$\dot{x} = \begin{bmatrix} 0 & 0 & 0 & 1 & 0 & 0 \\ 0 & 0 & 0 & 0 & 1 & 0 \\ 0 & 0 & 0 & 0 & 0 & 1 \\ 3\omega^2 & 0 & 0 & 0 & 2\omega & 0 \\ 0 & 0 & 0 & -2\omega & 0 & 0 \\ 0 & 0 & \omega^2 & 0 & 0 & 0 \end{bmatrix} x + \begin{bmatrix} 0 & 0 & 0 \\ 0 & 0 & 0 \\ 0 & 0 & 0 \\ 1 & 0 & 0 \\ 0 & 1 & 0 \\ 0 & 0 & 1 \end{bmatrix} u \tag{3.43}$$

3.5.1.3 Hill's State Transition Matrix

Hill's equations are in a linear form, thus they fit well to the linear systems toolset. If we assume a constant **A** over each discrete time step we can approximate

$$\Phi(t_{k+1}, t_k) = e^{(A\Delta t)} \tag{3.44}$$

$$\mathbf{A} = \left.\frac{\partial f}{\partial x}\right|_{\hat{x}_k} \tag{3.45}$$

This formulation provides a state transition matrix in linear form, that can be easily applied to both the state propagation steps and the covariance propagation.

3.5.2 Full Nonlinear Dynamic model

Although the relative dynamics are minimal in comparison between spacecraft, their actual perturbations on the dynamics are quite significant in LEO. In addition to increasing the fidelity of our dynamic model, it also allows us to customize the orbits and add other effects such as thruster firing, and differences in their drag coefficients.

3.5.2.1 Coordinate Frame

The coordinate frame used in the high fidelity dynamic model is the Earth Centered Inertial frame. This reference frame was chosen because it greatly simplifies the equations of motion.

The ECI coordinate system is also known as the IJK system. The $\hat{I}$ axis is

pointed towards the vernal equinox, the $\hat{J}$ axis is 90^o to the east along the equitorial plane, and the $\hat{K}$ axis extends through the north pole.

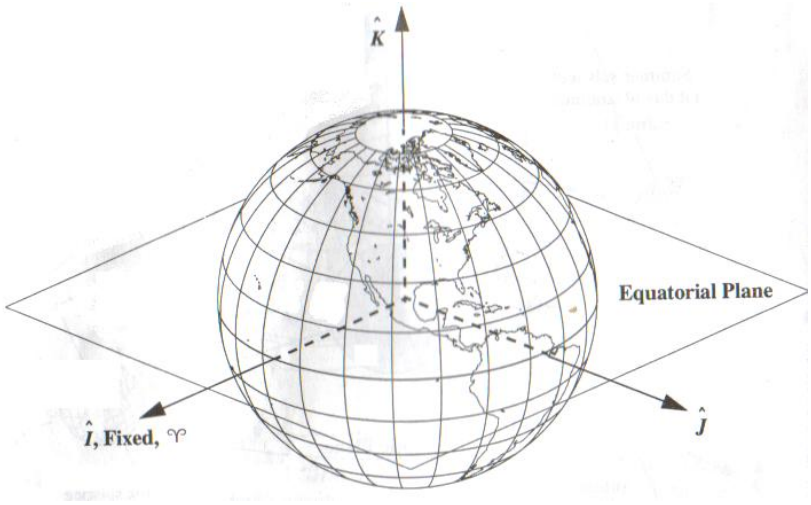

Figure 3.2: Earth Centered Inertial Frame[21]

3.5.2.2 Dynamic Equations

The full nonlinear dynamic equations are given by[1].

$$\ddot{r_x} = -\frac{\mu x}{r^3}\left[1 - \frac{3}{2}J_2\left(\frac{R_E}{r}\right)^2\left(\frac{5}{2}\frac{z^2}{r^2} - 1\right)\right] - \frac{1}{2}C_D\frac{A}{m}\rho V\left(\dot{x} + \omega_E y\right) \tag{3.46}$$

$$\ddot{r_y} = -\frac{\mu y}{r^3}\left[1 - \frac{3}{2}J_2\left(\frac{R_E}{r}\right)^2\left(\frac{5}{2}\frac{z^2}{r^2} - 1\right)\right] - \frac{1}{2}C_D\frac{A}{m}\rho V\left(\dot{y} + \omega_E x\right) \tag{3.47}$$

$$\ddot{r_z} = -\frac{\mu z}{r^3}\left[1 - \frac{3}{2}J_2\left(\frac{R_E}{r}\right)^2\left(\frac{5}{2}\frac{z^2}{r^2} - 3\right)\right] - \frac{1}{2}C_D\frac{A}{m}\rho V\dot{z} \tag{3.48}$$

The J_2 term is the zonal harmonic constant given by $1082.7x10^{-6}$. ω_E is the rotation rate of the earth, R_E is the radius of the earth, m is the objects mass, A is

the cross sectional area, and V is the relative wind. The relative wind is given by the equation

$$V = \sqrt{\dot{r}_x^2 + 2\omega_E \dot{r}_x r_y + \dot{r}_y^2 - 2\omega_E \dot{r}_y r_x + \omega_E^2 r_y^2 + \dot{r}_z^2} \tag{3.49}$$

The value of ρ is given by an exponential model derived in:

$$\rho = \rho_0 e^{(-a-a_o)/H} \tag{3.50}$$

Where $\rho_0 = 3.275e-12kg/m^3$, a is the current altitude, a_o is the reference altitude, $400000m$ and H is the scaling height $58515m$.

Now, using the form same from the simple GPS Kalman filter, choosing r as position and v as velocity. It is now appropriate to write these equations in terms of first order derivatives, to fit the canonical form, $\dot{r} = v$ and $\dot{v} = g(r, v)$. In this formulation, g is the nonlinear force model for the orbital dynamics. Now, let the state vector $x = [r, v]^T$.

$$\dot{x} = [v, g(r, v)]^T \tag{3.51}$$

or

$$f(x) = \begin{bmatrix} v_x \\ v_y \\ v_z \\ \ddot{r}_x \\ \ddot{r}_y \\ \ddot{r}_z \end{bmatrix} \tag{3.52}$$

Now the equations are in the appropriate form to apply the Kalman Filter. Since the Kalman filter's covariance propagation is a linear process, it is necessary to formulate the partial derivatives with repect to the state vector.

3.5.2.3 Partial Derivatives

This subsection lists the partial derivatives for the full nonlinear dynamic equations. Although the partials are not used to propogate the dynamics, they are needed when forming the state transition matrix for the covariance updates.

$$\frac{\partial \dot{r}_x}{\partial \dot{x}} = 1 \quad \frac{\partial \dot{r}_y}{\partial \dot{y}} = 1 \quad \frac{\partial \dot{r}_z}{\partial \dot{z}} = 1 \tag{3.53}$$

$$\begin{aligned} \frac{\partial \ddot{r}_x}{\partial x} = \quad & -\frac{\mu}{r^3}\left[1 - \frac{3}{2}J_2\left(\frac{R_E}{r}\right)^2\left(5\frac{z^2}{r^2} - 1\right)\right] \\ & +3\frac{\mu x^2}{r^5}\left[1 - \frac{5}{2}J_2\left(\frac{R_E}{r}\right)^2\left(7\frac{z^2}{r^2} - 1\right)\right] \\ & +\frac{1}{2}C_D\frac{A}{m}\rho V\frac{x(\dot{x}+\omega_E y)}{rH} \end{aligned} \tag{3.54}$$

$$+\tfrac{1}{2}C_D\tfrac{A}{m}\rho V\tfrac{x(\dot{x}+\omega_E y)(\dot{y}-\omega_E x)}{V}$$

$$\begin{aligned}\frac{\partial \ddot{r}_x}{\partial y} = \; & 3\tfrac{\mu xy}{r^5}\left[1-\tfrac{5}{2}J_2\left(\tfrac{R_E}{r}\right)^2\left(7\tfrac{z^2}{r^2}-1\right)\right] \\ & +\tfrac{1}{2}C_D\tfrac{A}{m}\rho V\tfrac{y(\dot{x}+\omega_E y)}{rH} \\ & -\tfrac{1}{2}C_D\tfrac{A}{m}\rho\left[V\omega_E+\tfrac{\omega_E(\dot{x}+\omega_E y)^2}{V}\right]\end{aligned} \tag{3.55}$$

$$\begin{aligned}\frac{\partial \ddot{r}_x}{\partial z} = \; & 3\tfrac{\mu xz}{r^5}\left[1-\tfrac{5}{2}J_2\left(\tfrac{R_E}{r}\right)^2\left(7\tfrac{z^2}{r^2}-1\right)\right] \\ & +\tfrac{1}{2}C_D\tfrac{A}{m}\rho V\tfrac{z(\dot{x}+\omega_E y)}{rH}\end{aligned} \tag{3.56}$$

$$\frac{\partial \ddot{r}_x}{\partial \dot{x}} = -\frac{1}{2}C_D\frac{A}{m}\rho\left[V+\frac{(\dot{x}+\omega_E y)^2}{V}\right] \tag{3.57}$$

$$\frac{\partial \ddot{r}_x}{\partial \dot{y}} = -\frac{1}{2}C_D\frac{A}{m}\rho\frac{(\dot{y}-\omega_E x)(\dot{x}-\omega_E y)}{V} \tag{3.58}$$

$$\frac{\partial \ddot{r}_x}{\partial \dot{z}} = -\frac{1}{2}C_D\frac{A}{m}\rho\frac{\dot{z}(\dot{x}+\omega_E y)}{V} \tag{3.59}$$

$$\begin{aligned}\frac{\partial \ddot{r}_y}{\partial x} = \; & 3\tfrac{\mu xy}{r^5}\left[1-\tfrac{5}{2}J_2\left(\tfrac{R_E}{r}\right)^2\left(7\tfrac{z^2}{r^2}-1\right)\right] \\ & +\tfrac{1}{2}C_D\tfrac{A}{m}\rho V\tfrac{x(\dot{y}+\omega_E x)}{rH} \\ & -\tfrac{1}{2}C_D\tfrac{A}{m}\rho\left[V\omega_E+\tfrac{\omega_E(\dot{y}+\omega_E y)^2}{V}\right]\end{aligned} \tag{3.60}$$

$$\begin{aligned}\frac{\partial \ddot{r}_y}{\partial y} = \quad & -\frac{\mu}{r^3}\left[1-\frac{3}{2}J_2\left(\frac{R_E}{r}\right)^2\left(5\frac{z^2}{r^2}-1\right)\right] \\ & +3\frac{\mu y^2}{r^5}\left[1-\frac{5}{2}J_2\left(\frac{R_E}{r}\right)^2\left(7\frac{z^2}{r^2}-1\right)\right] \\ & +\frac{1}{2}C_D\frac{A}{m}\rho V\frac{y(\dot{y}+\omega_E x)}{rH} \\ & +\frac{1}{2}C_D\frac{A}{m}\rho\frac{\omega_E(\dot{y}+\omega_E x)(\dot{x}-\omega_E y}{V}\end{aligned} \tag{3.61}$$

$$\begin{aligned}\frac{\partial \ddot{r}_y}{\partial z} = \quad & 3\frac{\mu xz}{r^5}\left[1-\frac{5}{2}J_2\left(\frac{R_E}{r}\right)^2\left(7\frac{z^2}{r^2}-1\right)\right] \\ & +\frac{1}{2}C_D\frac{A}{m}\rho V\frac{z(\dot{y}+\omega_E y)}{rH}\end{aligned} \tag{3.62}$$

$$\frac{\partial \ddot{r}_y}{\partial \dot{x}} = -\frac{1}{2}C_D\frac{A}{m}\rho\frac{(\dot{y}-\omega_E x)(\dot{x}+\omega_E y)}{V} \tag{3.63}$$

$$\frac{\partial \ddot{r}_y}{\partial \dot{y}} = -\frac{1}{2}C_D\frac{A}{m}\rho\left[V+\frac{(\dot{y}+\omega_E x)^2}{V}\right] \tag{3.64}$$

$$\frac{\partial \ddot{r}_y}{\partial \dot{z}} = -\frac{1}{2}C_D\frac{A}{m}\rho\frac{\dot{z}(\dot{y}+\omega_E z)}{V} \tag{3.65}$$

$$\begin{aligned}\frac{\partial \ddot{r}_z}{\partial x} = \quad & 3\frac{\mu xz}{r^5}\left[1-\frac{5}{2}J_2\left(\frac{R_E}{r}\right)^2\left(7\frac{z^2}{r^2}-3\right)\right] \\ & +\frac{1}{2}C_D\frac{A}{m}\rho V\frac{\dot{z}x}{rH} \\ & -\frac{1}{2}C_D\frac{A}{m}\rho\frac{\omega_E\dot{z}(\dot{y}-\omega_E x)}{V}\end{aligned} \tag{3.66}$$

$$\frac{\partial \ddot{r}_z}{\partial z} = \quad 3\frac{\mu yz}{r^5}\left[1-\frac{5}{2}J_2\left(\frac{R_E}{r}\right)^2\left(7\frac{z^2}{r^2}-3\right)\right] \tag{3.67}$$

$$+\tfrac{1}{2}C_D\tfrac{A}{m}\rho V\tfrac{\dot{z}y}{rH}$$

$$-\tfrac{1}{2}C_D\tfrac{A}{m}\rho\left(\tfrac{\omega_E\dot{z}(\dot{x}-\omega_E y)}{V}\right)$$

$$\begin{aligned}\frac{\partial\ddot{r}_z}{\partial z} = \quad & -\tfrac{\mu}{r^3}\left[1-\tfrac{3}{2}J_2\left(\tfrac{R_E}{r}\right)^2\left(5\tfrac{z^2}{r^2}-3\right)\right] \\ & +3\tfrac{\mu y^2}{r^5}\left[1-\tfrac{5}{2}J_2\left(\tfrac{R_E}{r}\right)^2\left(7\tfrac{z^2}{r^2}-5\right)\right] \\ & +\tfrac{1}{2}C_D\tfrac{A}{m}\rho V\tfrac{z\dot{z}}{rH}\end{aligned} \tag{3.68}$$

$$\frac{\partial\ddot{r}_z}{\partial\dot{x}} = -\frac{1}{2}C_D\frac{A}{m}\rho\frac{\dot{z}\left(\dot{x}+\omega_E y\right)}{V} \tag{3.69}$$

$$\frac{\partial\ddot{r}_z}{\partial\dot{y}} = -\frac{1}{2}C_D\frac{A}{m}\rho\frac{\dot{z}\left(\dot{y}+\omega_E x\right)}{V} \tag{3.70}$$

$$\frac{\partial\ddot{r}_z}{\partial\dot{z}} = -\frac{1}{2}C_D\frac{A}{m}\rho\left(V+\frac{\dot{x}^2}{V}\right) \tag{3.71}$$

3.5.2.4 State Transition Matrix

Hill's equations of motions are already in a convenient linear form: $\dot{x} = \mathbf{A}x + \mathbf{B}u$. The state transition matrix can simply be approximated by the matrix exponential $e^{\mathbf{A}\Delta T}$. This is given by the matlab command `expm(A*T)`. Where $\mathbf{A}$ is the linear system $\mathbf{A}$ matrix, and T is the time interval. In this particular implementation the time step is on the order of 1 second, thus T=1. This is both used in the dynamics, and the covariance propagation.

In the full nonlinear case the simulation would diverge after a few iterations using a first order approximation of the system. Instead, the state was integrated using MATLAB's `ode45` over time steps of one second. Since the covariance matrices must be propagated linearly, using, $\mathbf{P}_{k+1} = \mathbf{\Phi}(t_{k+1}, t_k)\mathbf{P}_k\mathbf{\Phi}(t_{k+1}, t_k)^T + \mathbf{Q}$. We also need to solve for $\mathbf{\Phi}$.

For a given linear system, we have:

$$\dot{\mathbf{\Phi}}(t_{k+1}, t_k) = \mathbf{A}(t_k)\mathbf{\Phi}(t_k) \tag{3.72}$$

That is, $\mathbf{\Phi}(t_{k+1}, t_k) = \int_{t_k}^{t_{k+1}} \mathbf{A}(\tau)\mathbf{\Phi} d\tau$ we should arrive at an approximate $\Phi(t_{k+1}, t_k)$. Since $\mathbf{A}$ is not constant over the time interval t_{k+1}, t_k, we cannot rely on the matrix exponential approximation for this integration.

In order to incorporate the variation of the states between time steps, the added dynamic equation $\dot{\mathbf{\Phi}} = \mathbf{A}\mathbf{\Phi}$ is included within the dynamic model propagation. This allows ode45 to integrate the dynamics *and* solve for $\mathbf{\Phi}$ between time steps, while varying $\mathbf{A}$ with the current state estimates.

In order to solve for $\mathbf{\Phi}$, ode45 requires the initial condition vector of the states, and the identity reshaped into a vector. The initial conditions fed into `ode45`. The resultant $\mathbf{\Phi}$ at the end of the integration is then used in the linear propagation of $\mathbf{P}$.

3.6 Measurement Connection Matrix for Hill's Model

Since Hill's model is in the relative frame, the shuttle's position is implicitly included in the states. Any paramters derived from the position, can be assumed to

be provided by GPS receiver's navigation solution

3.6.1 Differenced Reflected Pseudorange Measurement

The equation describing the reflected Pseudorange Measurement is given by:

$$h(X) = \rho_r = r_{sh} + r_{hg} - r_{gs} \tag{3.73}$$

The subscripts stand as the Shuttle to Hubble, Hubble to a GPS satellite, and A GPS satellite to the Shuttle respectively. The GPS satellites position is known from the ephemerides, and Shuttle's position is known from the receivers navigation solution. If we define, $\Delta_r = X_s - X_h$, that is the relative position between the Hubble and Shuttle and rotate into Hill's frame we arrive at:

$$\rho_r = |\Delta_r| + |\Delta_r - X_g| - |X_g| \tag{3.74}$$

Δ_r is our relative position vectory to Hubble in the ECI frame, and part of the state vector. Now taking partials with respect to Δ_r we arrive at:

$$\frac{\partial \rho_r}{\partial \Delta_r} = \frac{\Delta_r}{|\Delta_r|} + \frac{\Delta_r - X_g}{|\Delta_r - X_g|} \tag{3.75}$$

$$\frac{\partial \rho_r}{\partial \dot{\Delta}_r} = 0 \tag{3.76}$$

This forms our measurement vector:

$$H(x) = \begin{bmatrix} \frac{\partial \rho_r}{\partial \Delta_r}_{1x3} & \mathbf{0}_{1x3} \end{bmatrix} \tag{3.77}$$

3.6.2 Reflected Pseudorange Rate

The equation describing the reflected pseudorange rate measurement is given by:

$$h_{\dot{\rho}_r}(x) = \dot{\rho} = (V_s - V_h) \cdot \hat{los}_{sh} + (V_h - V_g) \cdot \hat{los}_{hg} \tag{3.78}$$

Now, substituting in the line of sight vectors:

$$\dot{\rho}_r = (V_s - V_h) \cdot \frac{X_s - X_h}{|X_s - X_h|} + (V_h - V_g) \cdot \frac{X_h - X_g}{|X_h - X_g|} \tag{3.79}$$

Now substituting in $\Delta_r = X_s - X_h$, and $\Delta_v = V_s - V_h$:

$$\dot{\rho} = \Delta_v \cdot \frac{\Delta_r}{|\Delta_r|} + (\Delta_v - V_g) \cdot \frac{\Delta_r - X_g}{|\Delta_r - X_g|} \tag{3.80}$$

Taking the partials with respect to the state Δ_r:

$$\frac{\partial \dot{\rho}}{\partial \Delta_r} = \Delta_v \cdot \left(\frac{1}{\Delta_r} - \frac{\Delta_r^2}{|\Delta_r|^3} \right) + (\Delta_v - V_g) \cdot \left(\frac{1}{|\Delta_r - X_g|} + \frac{\Delta_r - X_g}{|\Delta_r - X_g|^3} \right) \tag{3.81}$$

Now, taking the partials with respect to the state Δ_v:

$$\frac{\partial \dot{\rho}}{\partial \Delta_v} = \frac{\Delta_r}{|\Delta_r|} - \frac{\Delta_r - X_g}{|\Delta_r - X_g|} \tag{3.82}$$

Now to form the H vector:

$$H_{\dot{\rho}_r}(x) = \begin{bmatrix} \frac{\partial \dot{\rho}}{\partial \Delta_r} & \frac{\partial \dot{\rho}}{\partial \Delta_v} \end{bmatrix} \tag{3.83}$$

3.7 Measurement Connection Matrix for the Absolute Dynamic Model

The nonlinear measurements are given by the measurement equations. The measurement equation should be a function of the states of the system, such that $y = h(x)$.

In this formulation, there are 4 different measurements, pseudorange, differenced reflected pseudorange, pseudorange rate, and reflected pseudorange rate. In order to use these measurements in our Kalman filter design, we must linearize the measurements in order to form the canonical **H** matrix.

3.7.1 Direct Pseudorange measurement

The direct psuedorange measurement is given by the equation:

$$h_\rho(x) = \rho = r + c(t_u + \delta t + \delta t_D) \tag{3.84}$$

neglecting the ionospheric, receiver, ephemeris and other errors($\delta t + \delta T_d$), the measurement can expressed in terms of a range and bias.

$$h_\rho(x) = \rho = r + b = \sqrt{(x_s - x_g)^2 + (y_s - y_g)^2 + (z_s - z_g)^2} + b \tag{3.85}$$

where b is the receivers time offset(in meters) from the GPS constellation.

$$\mathbf{H}_\rho(x) = \frac{\partial \rho}{\partial x} \tag{3.86}$$

The partial with respect to the Shuttles position:

$$\frac{\partial \rho}{\partial x_s} = \frac{x_s - x_g}{(x_s - x_g)^2 + (y_s - y_g)^2 + (z_s - z_g)^2} \tag{3.87}$$

let $r_{sg} = \sqrt{(x_s - x_g)^2 + (y_s - y_g)^2 + (z_s - z_g)^2}$

Now taking it with respect to each position vector:

$$\begin{bmatrix} \frac{x_s - x_g}{r_{sg}} & \frac{y_s - y_g}{r_{sg}} & \frac{z_s - z_g}{r_{sg}} \end{bmatrix} \tag{3.88}$$

The partial with respect to the Shuttle's velocity:

$$\frac{\partial \rho}{\partial v_s} = \mathbf{0}_{1x3} \tag{3.89}$$

The partial with respect to receiver bias:

$$\frac{\partial \rho}{\partial r_b} = 1 \tag{3.90}$$

The partial with respect to Hubble's position:

$$\frac{\partial \rho}{\partial r_h} = \mathbf{0}_{1x3} \tag{3.91}$$

The partial with respect to Hubble's velocity:

$$\frac{\partial \rho}{\partial v_h} = \mathbf{0}_{1x3} \tag{3.92}$$

Now forming a H vector for the direct measurement

$$H_\rho(x) = \begin{bmatrix} \frac{\partial \rho}{\partial r_s}_{1x3} & \mathbf{0}_{1x3} & \mathbf{0}_{1x3} & \mathbf{0}_{1x3} & 1 \end{bmatrix} \tag{3.93}$$

3.7.2 Differenced Reflected Pseudorange measurement

The differenced reflected pseudorange provides information about the absolute shuttle and hubble position states. Its measurement equation is given as follows:

$$h(x) = \rho_r = r_{sh} + r_{hg} - r_{sg} \tag{3.94}$$

The bias terms difference out, as well as many of the other common mode errors greatly simplifying the calculation and the algebra. The subscripts sh, hg, and gs signify the range from shuttle to hubble, hubble to GPS transmitter, and shuttle to GPS transmitter.

These are equivalently:

$$r_{sh} = \sqrt{(x_s - x_h)^2 + (y_s - y_h)^2 + (z_s - z_h)^2} \tag{3.95}$$

$$r_{hg} = \sqrt{(x_h - x_g)^2 + (y_h - y_g)^2 + (z_h - z_g)^2} \tag{3.96}$$

$$r_{sg} = \sqrt{(x_s - x_g)^2 + (y_s - y_g)^2 + (z_s - z_g)^2} \tag{3.97}$$

Now, in order to form the H vector equation we must first linearize the measurement equation.

The partial with respect to the Shuttle's position:

$$\frac{\partial \rho}{\partial x_s} = \frac{x_s - x_h}{\sqrt{(x_s - x_h)^2 + (y_s - y_h)^2 + (z_s - z_h)^2}} - \frac{x_s - x_g}{\sqrt{(x_s - x_g)^2 + (y_s - y_g)^2 + (z_s - z_g)^2}} \tag{3.98}$$

substituting in the definitions of the range vectors we get:

$$\frac{\partial \rho}{\partial x_s} = \frac{x_s - x_h}{r_{sh}} - \frac{x_s - x_g}{r_{gs}} \tag{3.99}$$

Now extrapolating for each of the shuttle position components, we get a 1x3 vector

$$H_x = \begin{bmatrix} \frac{x_s - x_h}{r_{sh}} - \frac{x_s - x_g}{r_{gs}} & \frac{x_s - x_h}{r_{sh}} - \frac{x_s - x_g}{r_{gs}} & \frac{x_s - x_h}{r_{sh}} - \frac{x_s - x_g}{r_{gs}} \end{bmatrix} \tag{3.100}$$

The partial with respect to the Shuttle's velocity:

$$\frac{\partial \rho_r}{\partial \dot{x}_v} = \mathbf{0}_{1x3} \tag{3.101}$$

The partial with respect to the Shuttle's bias:

$$\frac{\partial \rho_r}{\partial \dot{x}_b} = 0 \tag{3.102}$$

The partial with respect to Hubble's position:

$$\frac{\partial \rho_r}{\partial x_h} = -\frac{x_s - x_h}{\sqrt{(x_s - x_h)^2 + (y_s - y_h)^2 + (z_s - z_h)^2}} + \frac{x_h - x_g}{\sqrt{(x_h - x_g)^2 + (y_h - y_g)^2 + (z_h - z_g)^2}} \tag{3.103}$$

Now substituting in the range definitions, and taking partials of HST's y and z components we arrive at the H vector:

$$\frac{\partial \rho_r}{\partial x_h} = \begin{bmatrix} -\frac{x_s - x_h}{r_{sh}} + \frac{x_h - x_g}{r_{hg}} & -\frac{y_s - y_h}{r_{sh}} + \frac{y_h - y_g}{r_{hg}} & -\frac{z_s - z_h}{r_{sh}} + \frac{z_h - z_g}{r_{hg}} \end{bmatrix} \tag{3.104}$$

The partial with respect to Hubble's velocity:

$$\frac{\partial \dot{r}_h}{\partial \rho_r} = \mathbf{0}_{1x3} \tag{3.105}$$

Now forming a H vector for the direct measurement

$$H_{\rho_r}(x) = \begin{bmatrix} \frac{\partial \rho}{\partial X_s}_{1x3} & \mathbf{0}_{1x3} & \frac{\partial \rho}{\partial X_h}_{1x3} & \mathbf{0}_{1x3} & 0 \end{bmatrix} \tag{3.106}$$

3.7.3 Pseudorange Rate measurement

The equation that relates the Pseudorange rate measurement to the states is given by:

$$h(x) = \dot{\rho} = (V_u - V_g) \cdot \frac{X_s - X_g}{|X_s - X_g|} \tag{3.107}$$

The measurement is simply the relative velocity along the line of sight vector between the GPS transmitter and the Shuttle.

$$H_{\dot{\rho}}(x) = \frac{\partial \dot{\rho}}{\partial X} \tag{3.108}$$

This partials with respect to the scalar x position is given as:

$\frac{\partial \dot{\rho}}{\partial x_s} = (V_s - V_g)_x \left[\frac{1}{\sqrt{(x_s - x_h)^2 + (y_s - y_h)^2 + (z_s - z_h)^2}} - \frac{(x_s - x_g)^2}{\sqrt{(x_s - x_h)^2 + (y_s - y_h)^2 + (z_s - z_h)^2}^3} \right]$

Now substituting in the range formulas to clean up

$$\frac{\partial \dot{\rho}}{\partial x_s} = (V_s - V_g)_x \left[\frac{1}{r_{sh}} - \frac{(x_s - x_g)^2}{r_{sh}^3} \right] \tag{3.109}$$

The same holds for the y and z vectors as well.

$$\frac{\partial \dot{\rho}}{\partial y_s} = (V_s - V_g)_y \left[\frac{1}{r_{sh}} - \frac{(y_s - y_g)^2}{r_{sh}^3} \right] \tag{3.110}$$

$$\frac{\partial \dot{\rho}}{\partial z_s} = (V_s - V_g)_z \left[\frac{1}{r_{sh}} - \frac{(z_s - z_g)^2}{r_{sh}^3} \right] \tag{3.111}$$

Now taking the partials with respect to range, it leaves us with simply the line of sight vectors.

$$\frac{\partial \dot{\rho}}{\partial V_s} = \frac{X_s - X_h}{|X_s - X_h|} \tag{3.112}$$

breaking these into components and substituting in the range equation, we get:

$$\frac{\partial \dot{\rho}}{\partial V_{s\,x}} = \frac{x_s - x_h}{r_s h} \tag{3.113}$$

$$\frac{\partial \dot{\rho}}{\partial V_{s\,y}} = \frac{y_s - y_h}{r_s h} \tag{3.114}$$

$$\frac{\partial \dot{\rho}}{\partial V_{s\,z}} = \frac{z_s - z_h}{r_s h} \tag{3.115}$$

Assuming a constant receiver bias:

$$\frac{\partial \dot{\rho}}{\partial X_b} = 0 \tag{3.116}$$

There is no information contained in the pseudorange rate about the state vector of the Hubble, hence the partials with respect to Hubble's states are 0.

$$\frac{\partial \dot{\rho}}{\partial X_h} = \mathbf{0}_{1x3} \tag{3.117}$$

$$\frac{\partial \dot{\rho}}{\partial V_h} = \mathbf{0}_{1x3} \tag{3.118}$$

Now constructing the H vector for the psuedorange rate measurement, we get:

$$H_{\dot{\rho}}(X) = \begin{bmatrix} \frac{\partial \dot{\rho}}{\partial X_s}_{1x3} & \frac{\partial \dot{\rho}}{\partial V_s}_{1x3} & \mathbf{0}_{1x3} & \mathbf{0}_{1x3} & 0 \end{bmatrix} \tag{3.119}$$

3.7.4 Reflected Pseudorange Rate measurement

The reflected pseudorange measurement is essentially the sum of the doppler shift along the paths of the signal. This is given by:

$$h(X) = \dot{\rho} = (V_s - V_h) \cdot \hat{los}_{sh} + (V_h - V_g) \cdot \hat{los}_{hg} \tag{3.120}$$

Now, expressing the line of sight vectors in terms of their components:

$$h(X) = \dot{\rho}_{rm} = (V_s - V_h) \cdot \frac{X_s - X_h}{|X_s - X_h|} + (V_h - V_g) \cdot \frac{X_h - X_h}{|X_h - X_g|} \tag{3.121}$$

From this, we need to take the partials with respect to the state vector components.

For the shuttle position states, in the x direction:

$$\frac{\partial \dot{\rho}}{\partial x_s} = (V_s - V_h)_x \left[\frac{1}{|X_s - X_h|} - \frac{(x_s - x_h)^2}{|X_s - X_h|^3} \right] \tag{3.122}$$

Now substituing in the range vectors to simplify the equation a little

$$\frac{\partial \dot{\rho}}{\partial x_s} = (V_s - V_h)_x \left[\frac{1}{r_{sh}} - \frac{(x_s - x_h)^2}{r_{hs}^3} \right] \tag{3.123}$$

For the shuttle position states, in the y and z directions:

$$\frac{\partial \dot{\rho}}{\partial y_s} = (V_s - V_h)_y \left[\frac{1}{r_{sh}} - \frac{(y_s - y_h)^2}{r_{hs}^3} \right] \tag{3.124}$$

$$\frac{\partial \dot{\rho}}{\partial z_s} = (V_s - V_h)_z \left[\frac{1}{r_{sh}} - \frac{(z_s - z_h)^2}{r_{hs}^3} \right] \tag{3.125}$$

Now taking the partial with respect to the Shuttle's velocity:

$$\frac{\partial \dot{\rho}}{\partial V_s} = \frac{X_s - X_h}{|X_s - X_h|} \tag{3.126}$$

This simply leaves us with the line of sight vector to the hubble; expanding this into the x,y, and z components:

$$\frac{\partial \dot{\rho}}{\partial V_{sx}} = \frac{x_s - x_h}{r_{sh}} \tag{3.127}$$

$$\frac{\partial \dot{\rho}}{\partial V_{sy}} = \frac{y_s - y_h}{r_{sh}} \tag{3.128}$$

$$\frac{\partial \dot{\rho}}{\partial V_{sz}} = \frac{z_s - z_h}{r_{sh}} \tag{3.129}$$

$$\frac{\partial \dot{\rho}}{\partial X_{hx}} = -(V_s - V_h)_x \cdot \left[\frac{1}{|X_s - X_h|} - \frac{(x_s - x_h)^2}{|X_s - X_h|^3} \right] + (V_h - V_g) \cdot \left[\frac{1}{|X_h - X_g|} - \frac{(x_h - x_g)^2}{|X_h - X_g|^3} \right] \tag{3.130}$$

substituting in the range vectors to clean up the equation, and extrapolating to the y,z vectors we arrive at:

$$\frac{\partial \dot{\rho}}{\partial X_{hx}} = -(V_s - V_h)_x \cdot \left[\frac{1}{r_{sh}} - \frac{(x_s - x_h)^2}{r_{sh}^3} \right] + (V_h - V_g)_x \cdot \left[\frac{1}{r_{hg}} - \frac{(x_h - x_g)^2}{r_{hg}^3} \right] \tag{3.131}$$

$$\frac{\partial \dot{\rho}}{\partial X_{hy}} = -(V_s - V_h)_y \cdot \left[\frac{1}{r_{sh}} - \frac{(y_s - y_h)^2}{r_{sh}^3}\right] + (V_h - V_g)_y \cdot \left[\frac{1}{r_{hg}} - \frac{(y_h - y_g)^2}{r_{hg}^3}\right] \quad (3.132)$$

$$\frac{\partial \dot{\rho}}{\partial X_{hz}} = -(V_s - V_h)_z \cdot \left[\frac{1}{r_{sh}} - \frac{(z_s - z_h)^2}{r_{sh}^3}\right] + (V_h - V_g)_z \cdot \left[\frac{1}{r_{hg}} - \frac{(z_h - z_g)^2}{r_{hg}^3}\right] \quad (3.133)$$

Now taking the partial with respect to the Hubble's velocity, we simply get a relation involving the ine of sight vectors.

$$\frac{\partial \dot{\rho}}{\partial V_h} = -\frac{X_s - X_h}{|X_s - X_h|} + \frac{X_h - X_g}{|X_h - X_g|} \quad (3.134)$$

expanding it into the x,y,z components and substituting in the range definitions we get:

$$\frac{\partial \dot{\rho}}{\partial V_{hx}} = -\frac{x_s - x_h}{r_{sh}} + \frac{x_h - x_g}{r_{hg}} \quad (3.135)$$

$$\frac{\partial \dot{\rho}}{\partial V_{hy}} = -\frac{y_s - y_h}{r_{sh}} + \frac{y_h - y_g}{r_{hg}} \quad (3.136)$$

$$\frac{\partial \dot{\rho}}{\partial V_{hz}} = -\frac{z_s - z_h}{r_{sh}} + \frac{z_h - z_g}{r_{hg}} \quad (3.137)$$

Since the reflected pseudorange rate does not involve the bias, it is simply 0.

$$\frac{\partial \dot{\rho}}{\partial X_b} = 0 \quad (3.138)$$

Now forming the linearized measurement vector:

$$H_{\dot{\rho}r}(X) = \begin{bmatrix} \frac{\partial \dot{\rho}r}{\partial X_s}_{1x3} & \frac{\partial \dot{\rho}r}{\partial V_s}_{1x3} & \frac{\partial \dot{\rho}r}{\partial X_h}_{1x3} & \frac{\partial \dot{\rho}r}{\partial V_h}_{1x3} & 0 \end{bmatrix} \tag{3.139}$$

3.8 Measurement Matrix

The measurement matrix corrects the Kalman Filter's dynamic estimates with the current measurement estimates. The measurement matrix is stacked up in the same order as the measurements.

The measurement for the relative filter is given by:

$$\mathbf{H} = \left[H_{\rho r}(X), H_{\dot{\rho}r}(X) \right]^T \tag{3.140}$$

The matrix for the Absolute dynamic filter is given as:

$$\mathbf{H} = \left[H_{\rho}(X), H_{\dot{\rho}}(X), H_{\dot{\rho}r}(X), H_{\dot{\rho}r}(X) \right]^T \tag{3.141}$$

3.9 The Process Noise Matrix

The process noise matrix, $\mathbf{Q}$ describes the covariance error associated with the model. It generally describes the model errors and unmodeled force inputs. In our case, since $\mathbf{Q}$ is difficult to obtain, it is treated as a tuning matrix, to adjust the performance of the filter.

3.9.1 Hill's Filter Process Noise Matrix

$$\mathbf{Q} = \begin{bmatrix} \sigma_p^2 \mathbf{I}_{3x3} & \mathbf{0}_{3x3} \\ \mathbf{0}_{3x3} & \sigma_v^2 \mathbf{I}_{3x3} \end{bmatrix} \tag{3.142}$$

σ_p is the standard deviation in Hill's relative position model, σ_v is the standard deviation in Hill's relative velocity model.

3.9.2 Absolute Dynamic Filter Process Noise Matrix

$$\mathbf{Q} = \begin{bmatrix} \sigma_{ps}^2 \mathbf{I}_{3\times3} & 0 & 0 & 0 & 0 \\ 0 & \sigma_{vs}^2 \mathbf{I}_{3\times3} & 0 & 0 & 0 \\ 0 & 0 & \sigma_{ph}^2 \mathbf{I}_{3\times3} & 0 & 0 \\ 0 & 0 & 0 & \sigma_{vh}^2 \mathbf{I}_{3\times3} & 0 \\ 0 & 0 & 0 & 0 & \sigma_b^2 \end{bmatrix} \tag{3.143}$$

σ_{ps} is the standard deviation in the Shuttle's position model, σ_{vs} is the standard deviation in the Shuttle's velocity model. σ_{ph} and σ_{vh} represent the standard deviation in Hubble's position and velocity models respectively.

3.9.3 The Measurement Noise Matrix

The $\mathbf{R}$ matrix represents the variance in the measurements. Ideally the variance is uncorrelated white gaussian noise. Since we can estimate the variance of the measurements with relative accuracy, this matrix is essentially fixed.

3.9.4 Hill's Measurement Noise Matrix

$$\mathbf{R} = \begin{bmatrix} \sigma_{\rho_r}^2 \mathbf{I}_{m\times m} & \mathbf{0}_{m\times m} \\ \mathbf{0}_{m\times m} & \sigma_{\dot{\rho}_r}^2 \mathbf{I}_{m\times m} \end{bmatrix} \tag{3.144}$$

$\sigma_{D\rho}$ and $\sigma_{D\dot{\rho}}$ are the differenced psuedorange and reflected pseudorange rate measurements.

3.9.4.1 Absolute Measurement Noise Matrix

$$R = \begin{bmatrix} \sigma_{\rho}^2 \mathbf{I}_{n\times n} & 0 & 0 & 0 \\ 0 & \sigma_{\dot{\rho}}^2 \mathbf{I}_{n\times n} & 0 & 0 \\ 0 & 0 & \sigma_{\rho_r}^2 \mathbf{I}_{m\times m} & 0 \\ 0 & 0 & 0 & \sigma_{\dot{\rho}_r}^2 \mathbf{I}_{n\times n} \end{bmatrix} \tag{3.145}$$

σ_{ρ} is the standard deviation in the pseudorange measurement, $\sigma_{\dot{\rho}}$ is the standard deviation in the pseudorange rate measurement. $\sigma_{D\rho}$ and $\sigma_{D\dot{\rho}}$ are the differenced psuedorange and reflected pseudorange rate measurements.

Chapter 4

The Experiment

4.1 Introduction

In September 2008, the next Hubble servicing mission, HST-SM4, will be flying to the Hubble Space Telescope in order to repair and replace critical parts on the telescope. The Shuttle will also be flying several experiments to try to perform relative ranging using a variety of sensors, such as the MDA camera for pose-estimation and ranging, and Goddard Space Flight Center's Navigator GPS receiver which will be recording direct and reflected GPS signals for a bi-static radar experiment.

4.1.1 The Hubble Space Telescope

The Hubble Space Telescope(HST) has been in service since 1990, it has provided astronomers with some of the clearest images yet to date. The next great telescope to be built is the James Webb Space Telescope, however, that is not due for launch until 2013.[16] During that time, the Hubble has had several serious onboard failures, particularly the gyros and main camera. HST-SM4 was originally scheduled for late 2004. However, due the the columbia disaster, the entire Shuttle fleet was grounded, practically ceasing all manned space flight operations and stopping all repair missions to Hubble.

Since the manned space option was no longer optional, there was a need for an autonomous servicing mission to repair the Hubble Space Telescope. This brought about many questions about relative navigation, rendezvous and docking. It became apparent, if there were to be future missions to service hubble, relative navigation would become an essential technology.

Since the return to flight and Dr. Mike Griffin's announcement to return to service Hubble, a manned servicing mission has been placed back into the Shuttle's manifest log. This planned mission is a continuation of the HST-SM4, however, it will now also include some relative navigation experiments to test the accuracy and viability of these sensors, algorithms, and techniques.

4.2 Overview of the Relative Navigation Sensor(RNS) Experiment

The primary purpose of the experiment is to record camera data from the MDA cameras to do pose estimation. One of the additional experiments is the bi-static radar experiment. It's primary goal is to record raw RF data from the Hubble during approach and docking. The GPS receiver will be powered on about at 1000 m from Hubble with the bay doors open, facing towards the aft end of Hubble. During approach the direct signals visible will be received by the RHCP GPS antenna. One of the nice features about a RHCP signal is that, when reflected off of a surface, it reverses polarization and becomes left hand circularly polarized. This gives it a nearly perfect rejection for a reflected signal. The aim of the experiment is the exploit this fact and use an LHCP Antenna to pick up these reflections.

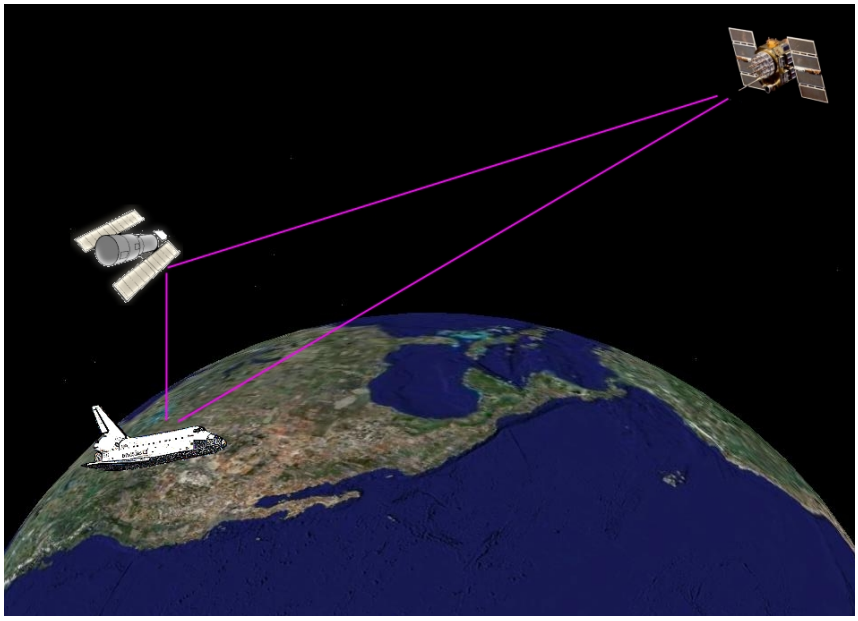

Figure 4.1: Simulation Geometry

Both of the antennae will be recording the raw RF stream mixed down to IF, 35.42 MHz, and then sampled at 8.192 MS/s. This data will be stored offline to a mass storage module and later brought to the ground for further processing.

Using faster computers and complex signal processing algorithms will be used to apply powerful filtering techniques and acquisition methods to determine the structure and composition of the reflected signals, including those too weak to be seen by a standard GPS receiver. One side benefit is that we are flying Goddard Space Flight Center's Navigator GPS receiver, built from the ground up, for space based weak signal acquisition and tracking. Navigator has a acquisition and tracking threshold 10 dB below the typical COTS receiver.

4.3 Hardware Specifications

The GPS receiver used to record the data is Goddard Space Flight Center's Navigator GPS receiver. The Navigator GPS reciever runs at 65.536 MHz using a General Dynamics Coldfire processor. It has 3 application specific Actel AX2000 FPGA's. Currently the GPS receiver is in development and the flight boards are being populated.

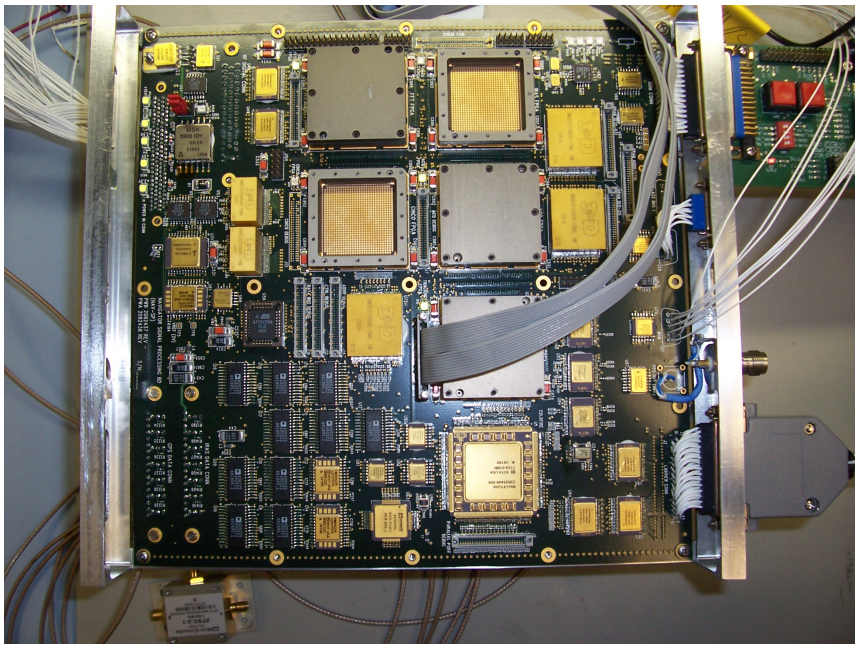

Figure 4.2: Navigator GPS Receiver Development Card

The enhanced capabilities of this receiver are aided by the application specific FPGAs that implement an algorithm developed by Dr. Mike Psiaki of Cornell and implemented in real time by Luke Winternitz from The University of Maryland. This algorithm is an FFT based acquisition algorithm that operates in the frequency domain. It is able to acquire and track signals down to 25 dB-Hz. This is approximately 10 dB more sensitive than current off the shelf GPS receivers.

This will enable Navigator to acquire the weaker reflections off of the Hubble Space Telescope.

The Navigator receiver will be configured to track 24 channels, 12 of them connected to the LHCP antenna and the remaining 12 connected to the RHCP antenna. If we are tracking a direct signal, the reflected channels will be directed to search in a time delayed space with approximately the same doppler frequency. This will aid our search for the weaker signals.

Onboard the Navigator, an extended Kalman filter will be running, using a paired down version of the Kalman filter represented here. This filter will be optimized for operation in a real time embedded environment. However, on the ground is is necessary to simulate and develop a filter first for this particular environment.

Chapter 5

Simulation

5.1 The Hubble Rendezvous

The Hubble Rendezvous truth-scenarios are chosen such that the initial conditions will result in a near collision of the Shuttle and Hubble. The 1st scenario implements a simple 2-body orbit propogator and uses PID feedback to "dock" with the Hubble to close their relative position magnitude to zero. This model is primarily used to determine the satellite visibility.

The latter scenario uses the same initial conditions, however, it also has a much higher fidelity orbit model. The high fidelity model is generated with STK using a high fidelity orbit propagator.

In the simulation, the Space Shuttle approaches Hubble from the aft end with its bay doors pointed towards Hubble. This allows the Shuttle to dock cleanly with Hubble.

During the servicing mission, the left and right handed GPS Antennae will be placed on the MULE inside the bay of the shuttle looking outwards.

The STK simulation focuses on simulating the uncontrolled motion of the two bodies. In order to represent the "docking", initial conditions were chosen such that the two space craft come within close proximity to eachother.

The simulation truth model was created using STK, given a set of inital condi-

Shuttle			Units
	ECI Position	$(-4673.7, -4525.4, 2443.5)^T$	Km
	ECI Velocity	$(5.604, -4.472, 2.438)^T$	Km/s
	Mass	109,000	kg
	Area	58.4	m^2
	C_d	1.2	
Hubble			
	ECI Position	$(-4673.9, -4525.9, 2443.7)^T$	Km
	ECI Velocity	$(-5.604, -4.471, 2.437)^T$	Km/s
	Mass	11,110	kg
	Area	15.4	m^2
	C_d	0.8	

Table 5.1: STK Parameters

tions, and propogated over an orbit period. The STK model chosen was a 21-order gravity model with atmospheric drag on both the Shuttle and Hubble, the coefficients of drag chosen as to represent the relative mass and area ratios.

The area for the Shuttle was approximated using the circular cross sectional area of the Shuttle[13]. The same was done for the Hubble.[16]

5.2 GPS Constellation Visibility

The visibility of each GPS satellite is determined by the geometry of the GPS constellation with respect to the location of Hubble and the Shuttle. The satellite visibility is essential to determining how many measurements, both direct and reflected are available. This number of measurements available influences the absolute and relative position accuracies.

5.2.1 Constellation Generation

The GPS constellation is constructed and propagated using the keplerian elements given by an almanac file. The almanac file is generated and uploaded to each GPS satellite. It represents a limited set of the keplerian orbits, in order to provide a rough position estimate of the GPS satellites. These orbits are then propagated in time, providing a good estimate of the satellites orbits. This is purely used to generate a moving rough estimate of the GPS constellation for the simulation.

In practice the GPS constellation is closely monitored, and each satellite has a new ephemeris updated every 3 hours. In addition to updating their GPS Almanac files every 12 hours.

The Almanac parameters are given by:

Parameter	Symbol	Scaling
Time of Almanac	toa	secs
Eccentric Anamoly	E	none
Inclination	$i0$	semicircles + 0.94247
Rate of Right Ascention	$\dot{\Omega}$	semicircles
Semi-major axis	$A^{\frac{1}{2}}$	none
longitude of perigee	λ	semicircles
Argument of Perigee	ω	semicircles
Mean Anamoly	M	semicircles

Table 5.2: Almanac

5.2.2 Earth Masking

Since we are only interested in observing those GPS Satellites with a reflected pair, and since the relative distance is so small, we can assume that any GPS satellite seen by the space Shuttle can also be seen by the Hubble.

The visible signals are done by masking out those GPS satellites who's main lobes cross through the earth, or are not in view of the shuttle. This is done by calculating the angle between the line of sight vector, and position vector of the shuttle. Lets call this angle β.

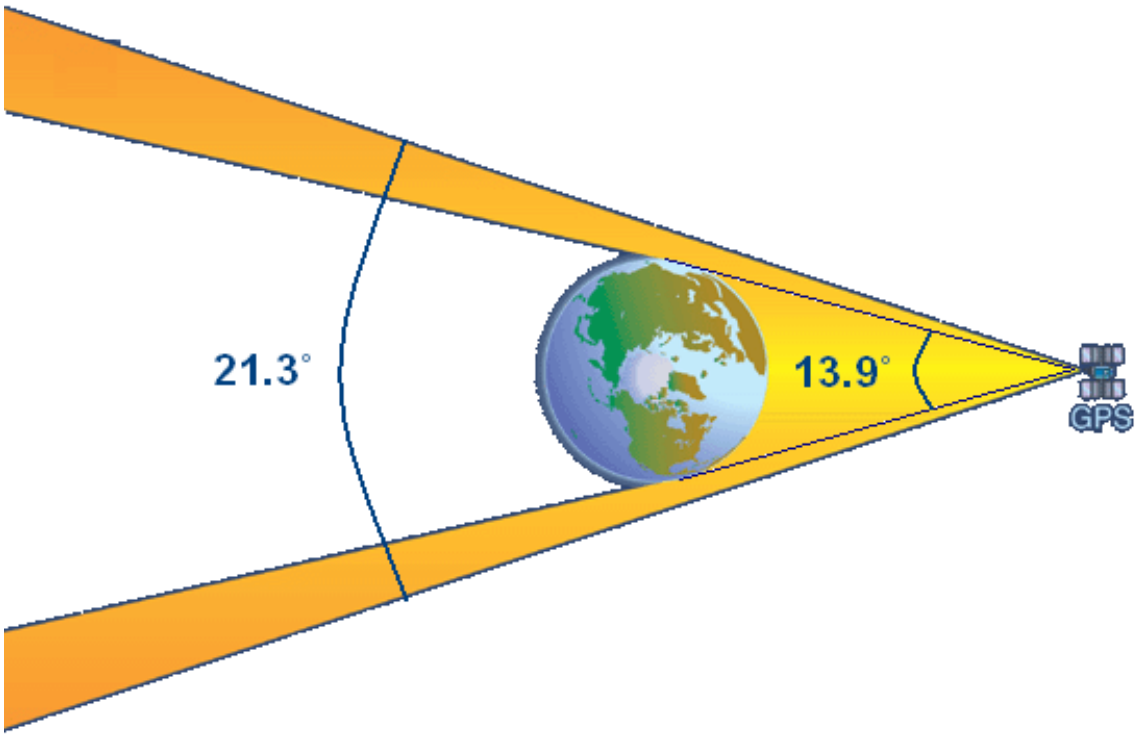

Figure 5.1: GPS Signal Masking

if β is greater than 13.9^o and less than 21.3^o then it is within the main lobe and just over the lim of the earth. If β is less than 13.9^o, then we need to check to make sure the signal does not pass through the earth. Thus, the dot product of the two vectors should be negative.

5.3 Signal Power Analysis

This section will describe the bistatic radar equation and the signal power analysis. It will also provide some preliminary plots showing the SNR and availible SV's with respect to a controlled docking scenario, i.e. the range closes perfectly to zero.

5.3.1 The Bi-Static Radar Equation

The bi-static radar equation described in [22] is given as:

$$(R_T R_R) = \left(\frac{P_T G_T G_R \lambda^2 \sigma_B {F_T}^2 {F_R}^2}{(4\pi)^2 K T_S B_N (S/N)_{min} L_T L_R} \right)^{1/2} \tag{5.1}$$

R_T	Transmitter to target range
R_R	Target to receiver range
P_T	Transmitter power
G_T	Transmit antenna power gain
G_R	Receive antenna power gain
σ_b	Bistatic radar cross section
F_T	Pattern propagation factor for transmit to target
F_R	Pattern propagation factor for receiver to target
K	Boltzman's constant
T_s	Receiver noise temperature
B_n	Noise bandwidth of the receivers pre-detection filter
(S/N)	signal-to-noise ratio required for detection
L_T	Transmit system losses
L_R	Receive system losses

Table 5.3: Bistatic Parameters

This equation is used to determine the maximum range to the target. However, rearranging terms, it is possible to pose this in the form of SNR received.

5.3.2 Universal Constants

There are several universal constants from this particular implementation. λ is the wavelength of the GPS L1 signal. The GPS L1 signal is transmitted at 1575.42 MHz, giving it a wavelength of 0.1903 m. Boltzmann's constant is given by $1.3806503x10^{-23}$ J/K. F_T and F_R are the pattern propagation factors, these factors describe the loss due to transmission in an unclean environment. F_T and F_R can be estimated at around 2 dB total for the ionospheric effects[14].

5.3.3 Bistatic Radar Cross Section

The bi-static radar cross section is calculated in much the same way as the standard radar cross section. However, the transmit angle needs to be taken into account, as well as properties limited only to the bi-static scenario.

5.3.3.1 Monostatic RCS Modeling

Since the Hubble can be approximated as a cylinder and the approach profile is towards the aft-end. The hubble can approximated by the reflective properties of a circular flat plate combined with a cylindrical surface normal to the flat plate. In physical optics, the equation describing the RCS for a metallic circular disk is described by[2].

$$\sigma = 16\pi \left| \frac{A\cos\theta}{\lambda} \cdot \frac{J_1(kd\sin\theta)}{kd\sin\theta} \right|^2 \tag{5.2}$$

Where A is given as the physical area of the disk, d is the diameter, and $J_1(x)$

is the bessel function of the first kind of order one. λ is the wavelength.

The Hubble space telescope has a diameter of roughly 4.2 m. Thus giving an area of roughly 13.85 m^2.

For normal incidence, this equation simplifies to:

$$\sigma = \frac{4\pi A^2}{\lambda^2} \tag{5.3}$$

This would represent the monostatic cross sectional area of the Hubble space telescope with the observer looking perpendicular to the aft end. Thus, the maximum possible cross-sectional area, looking at the aft end is 36.81 dB-sqm. It is interesting to note that the GPS signal will get gain from the reflections.

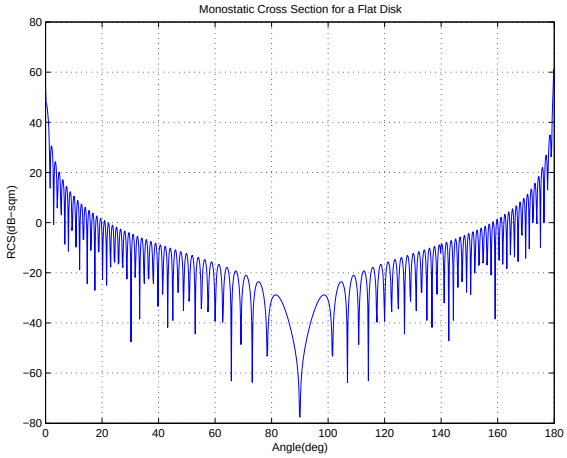

Figure 5.2: Monostatic Radar Cross Section for a Disk

If the observer was oriented perpendicular to Hubble, it would appear as a cylinder to the viewer. In this case, the RCS is given by:

$$\sigma = kal^2 \left| \frac{\sin(kl\sin(theta))}{kl\sin(theta)} \right|^2 \tag{5.4}$$

Where $a = 2.1m$ is the radius, $l = 14.2m$ is the length of the Hubble, k is

the wave number, and λ is the wavelength. This provides a radar cross section as follows:

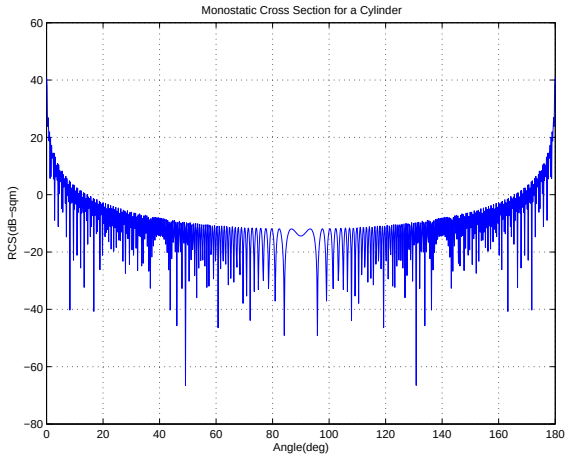

Figure 5.3: Monostatic Radar Cross Section for a Cylinder

Now, making the assumption since at the extremes of both of these figures, the RCS drops off significantly, and effectively take the maximum RCS. Of the two plots, the side of the cylinder offset by 90^o to form a combined RCS model for the cylinder over 180^o. Since a cylinder is symmetrical, this is effectively models the full cylinder over 360^o.

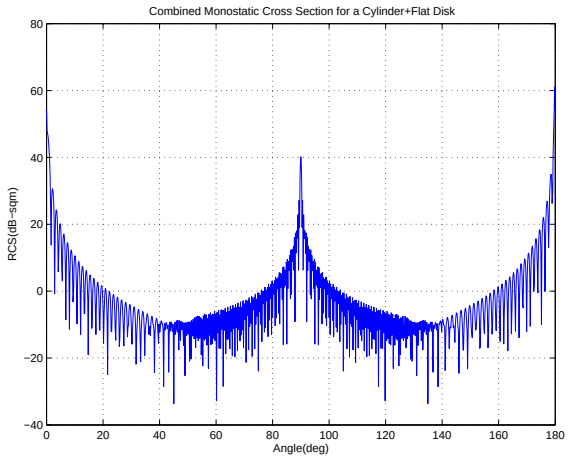

Figure 5.4: Combined Monostatic Radar Cross Section

5.3.3.2 Bi-static RCS Modeling

In order to account for the bi-static nature of the problem, it is necessary to define a new angle called the bi-static angle. This angle is defined as the difference between the receive and transmit antennae, $\beta = \theta_r - \theta_t$, the bisection of this angle is used to approximate the Bi-static RCS, σ_b

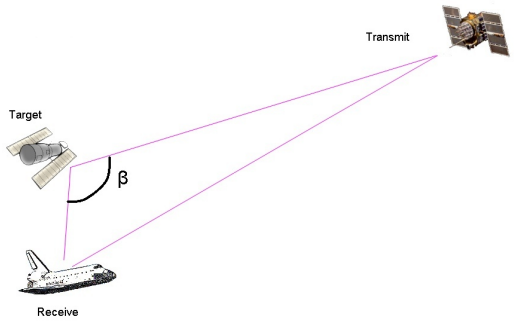

The bi-static RCS can be grouped into 3 sections: the psuedo-monostatic RCS region, the forward scatter RCS region, and the bi-static RCS region[22].

In the pseudo-monostatic region, the Crispin and Seigal monostatic-bi-static equivalence theorem predicts that for a sufficiently small angle, the RCS is equivalent to the monostatic RCS measured the bisector of the bistatic angle. This theorem applies to a sufficiently smooth surface, such as a sphere, a cylinder, or cone. Some empirical data for a cylinder, performed at 35 GHz, the pseudo-monostatic region extends to roughly 20^o, while the bistatic is within $20^o < \beta < 140^o$ and forward scatter at $\beta > 140^o$[22].

The bi-static region begins where the pseudo-monostatic region ends, it is where the theorem fails to predict an accurate RCS. Unfortunately, there is no

empirical formula for this equation. Experimental data shows a downward trend, from -2 dB to -15 dB, in this case. It should suffice to use a linear approximation(in dB).

The third bi-static region is the forward scattered region, this occurs when the bi-static angle approaches 180^o. The forward scatter can be approximated by treating the shadow area as a uniformly illuminated antenna aperture. The rolloff can be approximated when $\pi - \beta$ is substituted for the angle off aperture normal. This function closely matches $\frac{J_0(x)}{x}$ where $J_0(x)$ is the bessel function of order 0.[22] In our situation, many of the GPS satellites will lie in this area, due to being below the constellation. This is to our benefit, allowing us to pick up signals, being at such an odd orientation. Luckily due to the change in polarization of the reflected signal, this will provide us with isolation from the direct signal from the satellite.

From these bi-static regions we can now form a full approximation for the bi-static radar coefficient. The plot below represents σ_b with the flat face of the cylinder oriented towards the receiver.

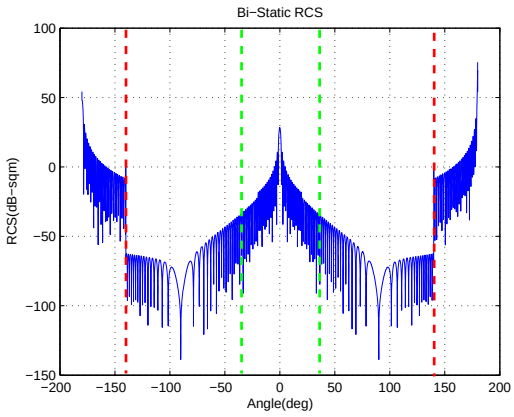

Figure 5.5: Bi-Static Radar Cross Section: This plot depicts the bi-static radar cross section, with the receiver facing the front end of a cylinder. The green line represents the transition between the pseudomonostatic region and the bi-static region. The red line represents the transition to the forward scattering region.

This approximation closely matches the experimental plots given in [22], while the experimental data uses a different sized cylinder, and different wavelength, of 1.85 cm(35 GHz) respectively, they are very similar in ratio. This should provide a reasonable fit for a perfectly reflecting disk.

5.3.4 Antenna Gain

The antennae chosen for this mission are two hemispherical antennas. The antenna gain is given as 3 dBic. Built into each antenna is the low noise amplifier. The LNA has a gain of 26 dB with a noise figure of 2.8. This can be used to calculate the system noise temperature. This equation is given as:

$$T_s = 10\log(T_A(NF-1)) \tag{5.5}$$

Where, T_A is the temperature at the antenna. Since the LNA is at the antenna, the line losses are included in the analysis. From the spec sheet, the NF of the

antenna is given as 2.8 dB. A conservative approximation for this noise figure is to use the temperature at the antenna, T_A, as room temperature or 290 K. This approximation holds because the antennae are lying on the MULE. The MULE will be heated in order to keep the electronics from freezing. From this equation we find that the receiver noise temperature is 24.4 dB-K.

The antenna gain is given by [19], however since it is hemispherical, we can assume a uniform 3 dB of gain.

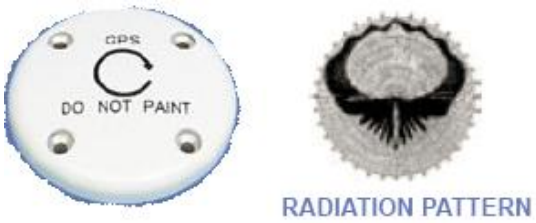

Figure 5.6: Antenna Pattern

5.3.5 Design Constants

The L_R and L_T and receiver and transmit system losses respectively will be taken into account as a total system loss. A general approximation of loss in a communications system is about 2 dB. Usually this value is measured quantitatively, but, without a complete system to test, it is difficult to arrive at a true figure. The noise bandwidth, B_n is generally taken as $1/T$, where T is the pre-integration period. For Navigator, it has an adjustable preintegration period, however the nominal case is 1 ms. Other losses occur such as Polarization mismatch contributing 3 dB [14] and in the case of a reflection, there is a efficiency which is dependant on the reflectivity of the object. In the case of the Hubble, which is coated in mylar, it will have a

high reflectivity coefficient, this is typically 90-98%, depending on the quality. For the sake of this arguement, lets assume a loss of 0.2 dB or roughly 95% reflectivity.

5.3.6 Range Calculation

The range calculations are performed as described in Chapter 6. R_R is simply the geometric distance between the Shuttle and the Hubble, while R_T is simply the geometric distance between each GPS Satellite and the Hubble. Factoring the free space loss due to range the equations:

$$R_T(dB) = 20\log(\frac{4\pi R_T}{\lambda}) \tag{5.6}$$

$$R_R(dB) = 20\log(\frac{4\pi R_R}{\lambda}) \tag{5.7}$$

The plot below shows the ranges from each GPS Satellite to the Hubble. The discontinuities come from satellites dropping in and out of view.

5.3.7 Transmit Power

The exact GPS satellite transmit powers are proprietary information and not publically available. However [14] calculates the required Satellite EIRP. This value is given as 26.8 dBW This is the minimum power transmitted by each GPS Satellite. The EIRP includes both the G_T and P_T.

5.4 Signal to Noise Analysis

At each time-step, for each visible GPS satellite, we calculate each range value. Now, making the assumption that the Shuttle is oriented with its bay doors towards the aft bulkhead of Hubble, it is possible to estimate the angle β and which surface of the cylinder the reflection is striking. The truth positions were generated from a file that is the simple 2-body relative motion, coupled with some thruster firing for a realistic closing profile. This produces an expected expected satellite visibility given the aforementioned conditions. It should be noted that the model does not take into account the reflections from the solar panels and assumes an orientation with the antennae directly facing the aft bulkhead.

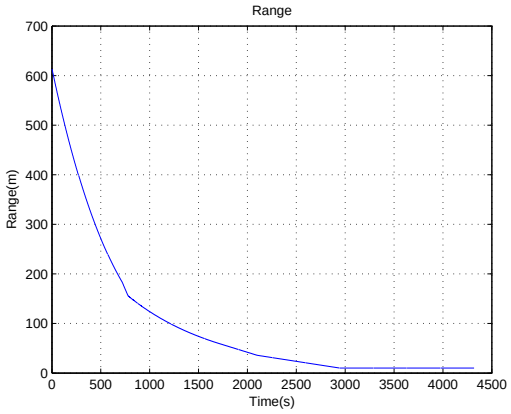

Figure 5.7: Relative Position Magnitude for the "docking" scenario

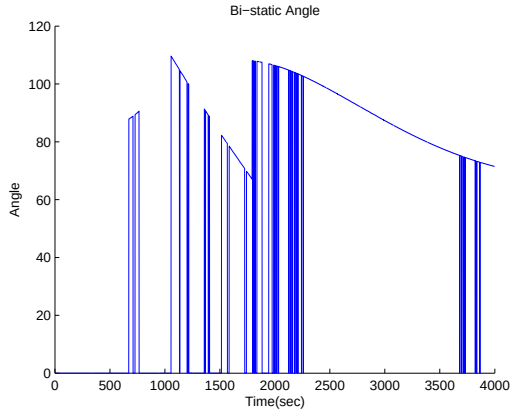

Figure 5.8: Reflected Received Angle,β: Received bi-static angles from a GPS Satellites. This is a typical bi-static angle for a given GPS Satellite over the docking. The discontinuity is when the satellite drops out fo view, and the next visible satellite moves into place. Notice that it is primarily in the "bi-static" region, that is, the location where the signal power is weakest.

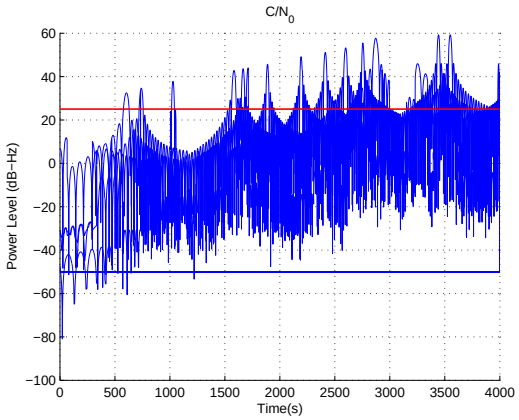

Figure 5.9: Reflected Received CN0 - The red line represents Navigator's current acquisition threshold of 25 dB-Hz. Typical receiver performance is evaluated by calculating the Carrier to Noise ratio, this is given by the signal seen at the A/D's. This is calculated simply by adding 30 dB-Hz to the SNR($10\log_1 0(\tau_{chip})$ where τ_{chip}=1023 chips/sec

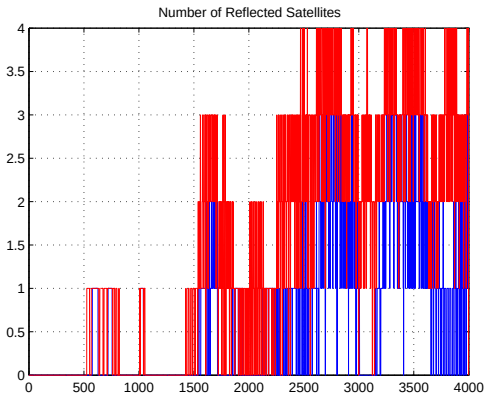

Figure 5.10: The blue line represents the number of visible satellites at each time step as seen by a receiver with 25 dB-Hz sensitivity. The red plot represents the number of satellites visible, if the receivers sensitivty was increased by 10 dB. Clearly, the a more sensitive receiver will be able to see a greater amount of reflections.

5.5 Average Signal Visibility

It is necessary to establish a baseline of the expected signal visibility. In order to avoid any pathological problem due to a bad simulation geometry, several variations have to be run to determine if the signal power levels, and visibility are realistic. The plot below shows the average signal visibility for reflected signals, and direct signals $\pm$ one standard deviation. This demonstrates the expected satellite visibility while varying the GPS Constellation. This figure is averaged over 20 runs, randomly varying the GPS constellation in its 12 hour orbit. As expected the number of reflected satellites increases dramatically as you approach the Hubble. The drop-off towards the end of the run is due to the approximation of the bistatic angle where the assumptions about the relative attitude begins to break down.

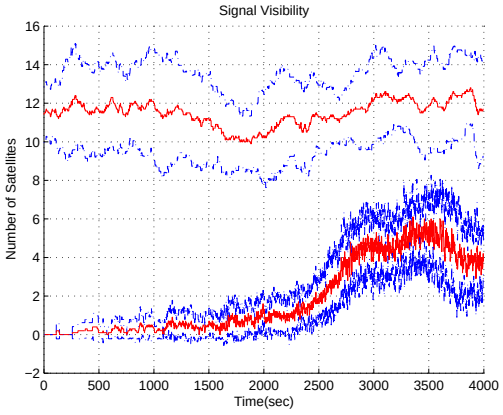

Figure 5.11: Number of Visible Satellites averaged over 20 runs. The top red line represents the number of direct GPS Signals. The bottom red line represents the number of reflected satellites. The blue envelopes represent the $\pm 1 - \sigma$.

5.6 Measurement Generation

The measurements in the simulation were generated at each time step using the truth positions to calculate the relative path lengths between each spacecraft. These pathlengths were used to determine which signal was visible and strong enough for reception. After selecting the viable signals, the measurements were constructed from the geometry.

5.7 Direct Pseudorange Measurements

The direct signal is generated using the truth positions of the Shuttle and Hubble. A reciever bias is added on top of the signal, as well as the ionospheric error given by the equation below[1]:

$$\delta_{iono} = \frac{82.1TEC}{F_C^2\sqrt{\sin^2(EL) + 0.76} + \sin^2(EL)} \tag{5.8}$$

TEC is the total electron content, given by 2e17. F_c is the carrier frequency 1.57542 GHz, and EL is the elevation of the GPS satellite over the horizon.

The direct signal pseudorange rate is generated by the rate of change of the line of sight vectors. In practice, most GPS receivers rely only on the pseudorange measurements or use carrier phase to generate the velocities. The pseudorange rate measurements are generally noisy and actually degrade the performance of the filter.

A variance of 5 meters was chosen for the direct pseudo-ranges, and 25 cm/s for the psuedo-range rates. It is composed of the clock drift, ephemeris errors, phase noise, and other unmodeled sources. These values are based on the measured performance on the Navigator GPS receiver in a LEO simulation. The signals were generated in the same way, as described in Chapter 2. The ionospheric bias was neglected in this simulation, as it would have been differenced out in the measurement generation. Instead, the pseudo-range variance was increased by a nominal amount, 0.25 m, to reflect the ionospheric model discrepencies.

5.8 Differenced Reflected Measurements

The differenced reflected measurements were constructed from the total path lengths between the GPS Satellite, Hubble, and the Shuttle. The noise added is from the loss in signal quality due to the reflective properties and small ionospheric error. Since the measurement is a differenced reflected signal with that of the direct

path, the bias and the the ionospheric terms become small and are negligible. In addition to the ionospheric error practically canceling out, the front end bias, clock bias, thermal jitter and other common mode errors also disappear.

A variance of 25 meters was chosen for the reflected pseudo-ranges, and 50 cm/s for psuedo-range rates. Although the true variance is unknown, it is extremely difficult to model on the earth. Future tests will include an anechoic chamber testing or data reduction of the rendezvous experiment. The signals were generated in the same way, as described in Chapter 2.

Chapter 6

Scenarios

6.1 Introduction

This chapter illustrates the results of several interesting scenarios. The first scenario examined is purely the simple navigation filter. Then, each feature is incrementally added on, to demonstrate the added value. The latter sections demonstrate the effects of the inclusion of the new bi-static radar measurements and analyze their performance as a whole on the relative navigation system. All error values are given as the mean plus/minus the standard deviation($\mu \pm \sigma$).

6.2 Shuttle Navigation Filter

This section addresses the Shuttle navigation Kalman filter. It examines the simple position/velocity filter, and the more complicated orbital dynamics model.

6.2.1 Signal Visibility

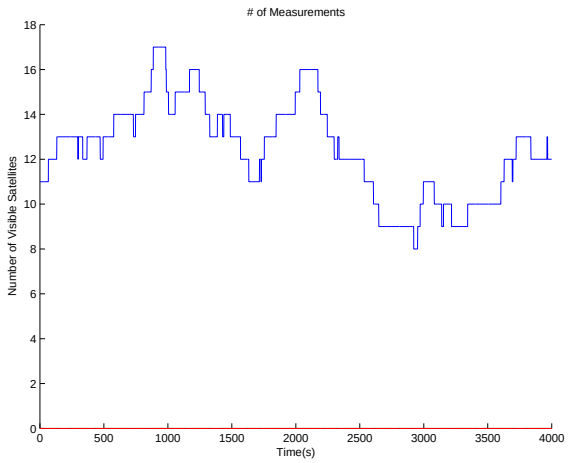

Figure 6.1: No Reflected Signal Visibility Plot: This plot shows the number of visible direct GPS signals availible

6.2.2 Simple Kalman Filter

6.2.2.1 Shuttle States

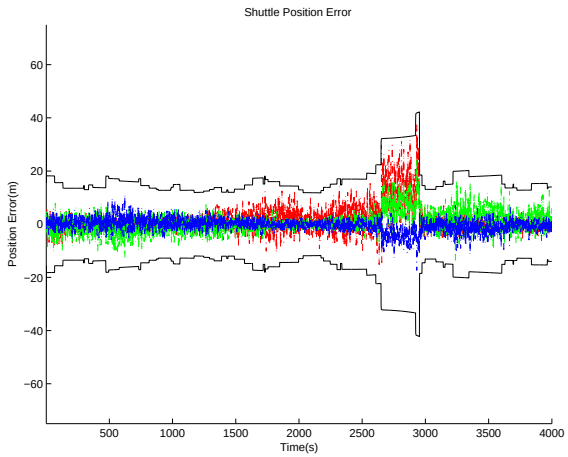

Figure 6.2: No Visibility Shuttle Position Error: This plot shows the time evolution of Shuttle's position error in the ECI coordinate frame. The black lines represent the 3d-err covariance errors, while the red,green, and blue are the errors along I, J, and K vectors respectively. The 3d-err error is: 6.18 m mean and 5.99 m standard deviation.

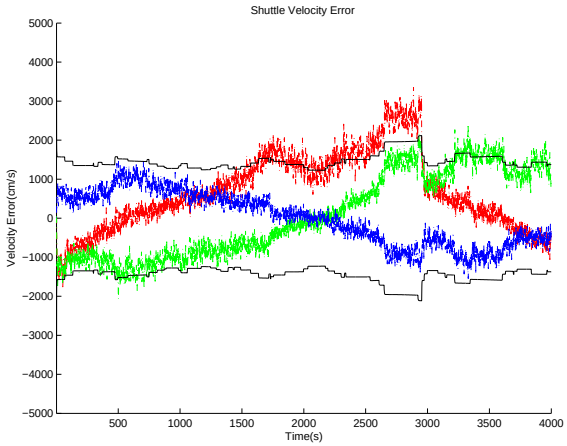

Figure 6.3: No Visibility Shuttle Position Error: This plot shows the time evolution of Shuttle's position error in the ECI coordinate frame. The black lines represent the 3d-err covariance errors, while the red,green, and blue are the errors along I, J, and K vectors respectively. The 3d-err error is: 1863 cm/s mean and 667 cm/s standard deviation.

6.2.2.2 Discussion

The filter performs decently enough, however, the weighting in the measure-meants makes it heavily sensitive to outages, or signal visibility issues. The large valued **Q** matrix effectively puts the dynamic part of the filter to sleep.

		Position σ	Velocity σ
Shuttle			
	$\hat{I}$	2.591±6.131 m	964.908±1039.089 cm/s
	$\hat{J}$	2.092±4.146 m	1031.988±603.971 cm/s
	$\hat{K}$	-1.210±2.601 m	-588.621±363.102 cm/s
	3d-err	6.182±5.988 m	1863.614±667.253 cm/s

Table 6.1: Simple Kalman Filter with Full Signal Avalibility

6.2.2.3 Configuration

The **Q** matrix for the dynamic filter needed to be increased compared to the high fidelity filter. This increases the weighting on the measurements and effectively put the dynamics to sleep. The values of **Q** were chosen to be $\sigma_p \mathbf{I} = 1e-2, \sigma_v \mathbf{I} = 1e-5, \sigma_b = 5$.

6.2.3 High Fidelity Kalman Filter

This simulation is of the high fidelity Kalman filter propagating the absolute state of the Shuttle. This filter is using only using the direct measurements, pseudorange and pseudorange rate, to determine the absolute position of the Shuttle. The same satellite visibility profile was used.

6.2.3.1 Shuttle States

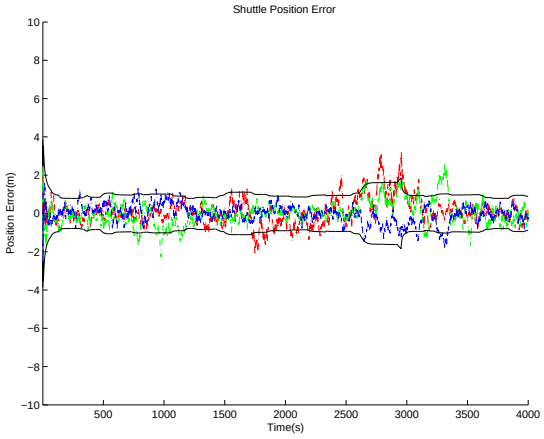

Figure 6.4: Shuttle Position Error: This plot shows the time evolution of Shuttle's position error in the ECI coordinate frame. The black lines represent the 3d-err covariance errors, while the red,green, and blue are the errors along I, J, and K vectors respectively. The 3d-err error is: 0.988 m mean and 0.709 m standard deviation.

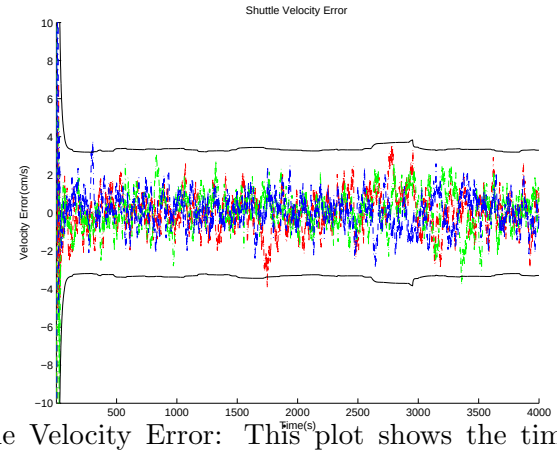

Figure 6.5: Shuttle Velocity Error: This plot shows the time evolution of Shuttle's position error in the ECI coordinate frame. The black lines represent the 3d-err covariance errors, while the red,green, and blue are the errors along I, J, and K vectors respectively. The 3d-err error is: 1.589 cm/s mean and 0.780 cm/s standard deviation.

6.2.3.2 Discussion

The filter performs reasonably well. The Q matrix could be tightened up a little, ,however, this is relaxed to prevent it from diverging during outages or poor visibility conditions. It shoudl be noted that there is a dynamic mismatch in the drag term, which causes a "bump" in the solution.

		Position $\mu \pm \sigma$	Velocity $\mu \pm \sigma$
Shuttle			
	$\hat{I}$	0.270±0.797 m	0.172±1.065 cm/s
	$\hat{J}$	0.247±0.668 m	0.103±1.069 cm/s
	$\hat{K}$	-0.214±0.467 m	-0.045±0.904 cm/s
	3d-err	0.988±0.709 m	1.589±0.780 cm/s

Table 6.2: High Fidelity Shuttle Simulation with full signal avalibility

6.2.3.3 Configuration

The **Q** matrix for the dynamic filter was adjusted until the covariance bars were relatively close to the dynamics, while keeping the filter stable. This increases the weighting on the dynamics and uses them to propagate the position. The values of **Q** were chosen to be $\sigma_p = 1e-3, \sigma_v = 1e-5, \sigma_b = 10$.

6.3 No Reflected Measurements

The results presented in this section rely on purely dynamic model and direct measurements to formulate the relative position. The initial conditions are set, such that the relative position and velocity of the Hubble is known to within 1%, at the start of the filtering process.

6.3.1 Signal Visibility

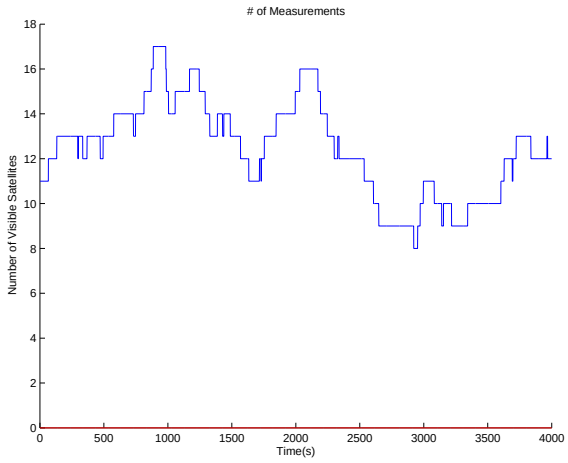

Figure 6.6: No Reflected Signal Visibility Plot: This plot shows the number of visible direct GPS signals availible

6.3.2 High Fidelity Filter

In this scenario, the high fidelity filter is propagating the absolute states. The Hubble states are without measurement inputs and our dynamics are free running.

6.3.2.1 Shuttle States

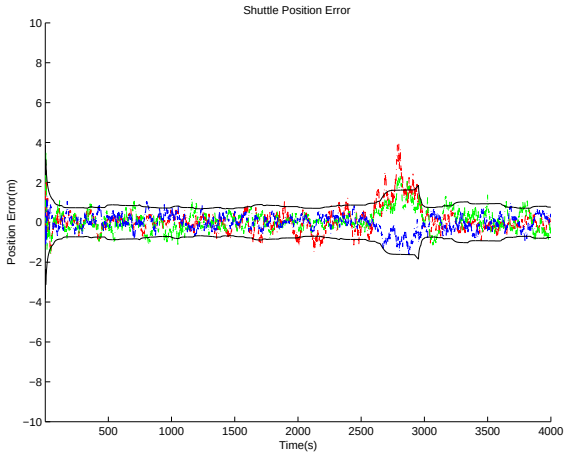

Figure 6.7: No Visibility Shuttle Position Error: This plot shows the time evolution of Shuttle's position error in the ECI coordinate frame. The black lines represent the 3d-err covariance errors, while the red,green, and blue are the errors along I, J, and K vectors respectively. The 3d-err error is: 0.898 m mean and 0.703 m standard deviation.

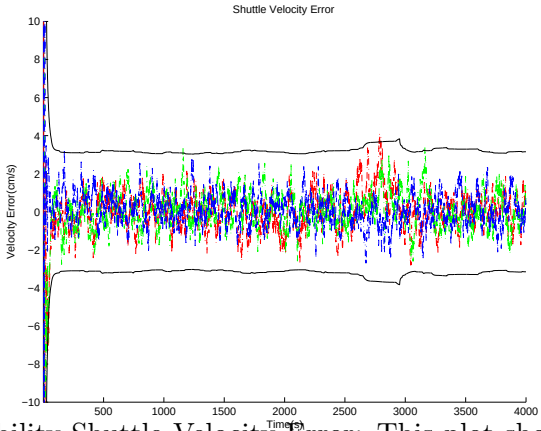

Figure 6.8: No Visibility Shuttle Velocity Error: This plot shows the time evolution of Shuttle's velocity error in the ECI coordinate frame. The black lines represent the 3d-err covariance errors, while the red,green, and blue are the errors along I, J, and K vectors respectively. The 3d-err error is: 1.479 cm/s mean and 0.718 cm/s standard deviation.

6.3.2.2 Hubble States

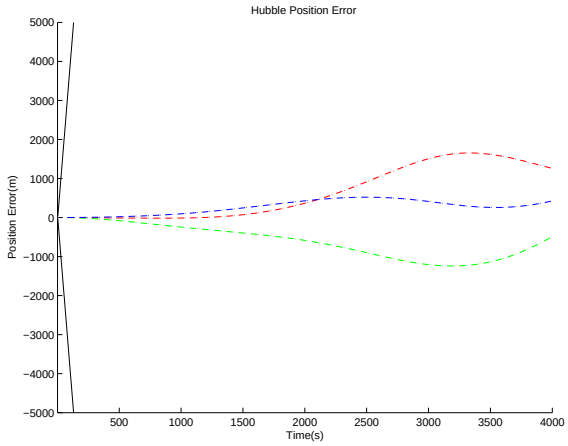

Figure 6.9: No Visibility Hubble Position Error: This plot shows the time evolution of the HST's position error in the ECI coordinate frame. The black lines represent the 3d-err covariance errors, while the red,green, and blue are the errors along I, J, and K vectors respectively. The 3d-err error is: 17933 m mean and 8633 m standard deviation.

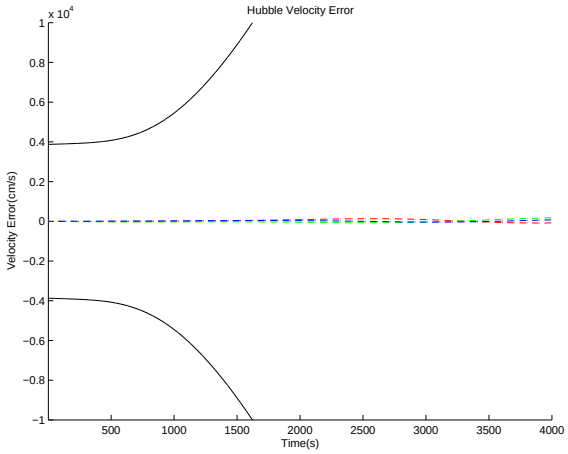

Figure 6.10: No Visibility Hubble Velocity Error: This plot shows the time evolution of the HST's velocity error in the ECI coordinate frame. The black lines represent the 3d-err covariance errors, while the red,green, and blue are the errors along I, J, and K vectors respectively. The 3d-err error is: 1651 cm/s mean and 806 cm/s standard deviation.

6.3.2.3 Discussion

Since the direct measurements feed into the shuttle's state estimate, we are able to solve for a position solution and resolve the Space Shuttle's position to within

5 to 10 meters. Having no reflected measurements in this model cause the states to be freely propagated. Thus as the time goes on, the states begin to diverge without the measurements to correct the state.

		Position $\mu \pm \sigma$	Velocity $\mu \pm \sigma$
Shuttle			
	$\hat{I}$	0.204±0.815 m	0.225±1.036 cm/s
	$\hat{J}$	0.232±0.571 m	0.059±0.917 cm/s
	$\hat{K}$	-0.116±0.448 m	-0.021±0.858 cm/s
	3d-err	0.898±0.703 m	1.479±0.718 cm/s
Hubble			
	$\hat{I}$	12822.475±7646.090 m	1056.633±644.297 cm/s
	$\hat{J}$	10293.770±2102.966 m	376.443±81.715 cm/s
	$\hat{K}$	-4812.628±6304.312 m	-1066.342±750.003 cm/s
	3d-err	17933.489±8633.910 m	1651.813±806.793 cm/s

Table 6.3: No Visibility ECI Error Table: This table lists the mean errors $/pm$ the standard deviation for each respective coordinate, and the 3d-err position for the zero-visibility case

6.3.3 Hill's Filter

Since there are no reflections in Hill's filter the states are allowed to evolve without input. It is clear that without any measurement corrections, Hill's model begins to diverge. Once after roughly 2000 seconds, in the STK model, the two

orbiters begin moving further apart, and Hill's linearization begins to break down. Hence, the drastic increase in position error as the relative distance increases.

6.3.3.1 Relative State Errors

The relative state errors are given in relative ECI position errors.

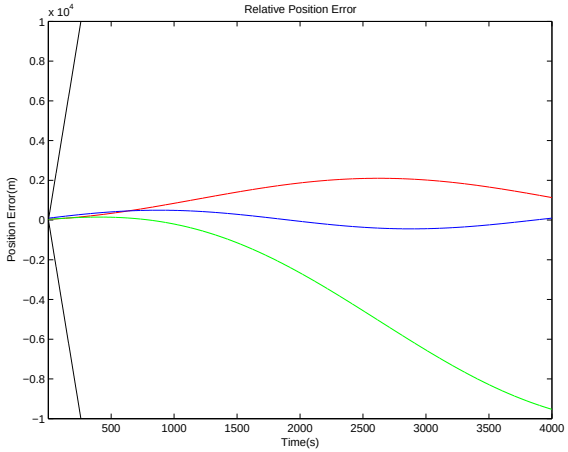

Figure 6.11: No Visibility RIC Position Error: This plot shows the time evolution of the RIC position vector in hill's frame. The black lines represent the 3d-err covariance errors, while the red,green, and blue are the errors along R, I, and C vectors respectively. The 3d-err error is: 3976 m mean and 3112 m standard deviation.

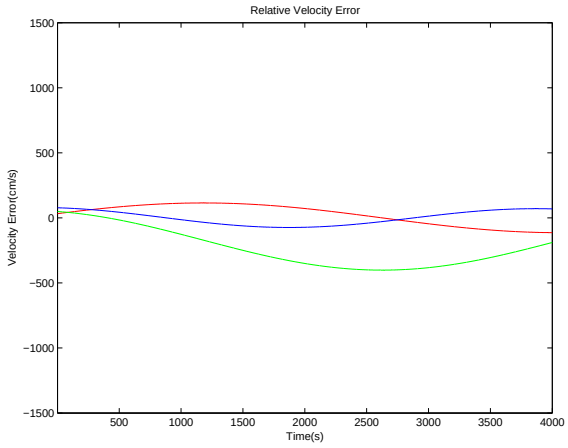

Figure 6.12: No Visibility RIC Velocity Error: This plot shows the time evolution of the RIC velocity vector in hill's frame. The black lines represent the 3d-err covariance errors, while the red,green, and blue are the errors along R, I, and C vectors respectively. The 3d-err error is: 274 cm/s mean and 110 cm/s standard deviation.

6.3.3.2 Discussion

	Position $\mu \pm \sigma$	Velocity $\mu \pm \sigma$
Radial	1835.085±280.315 m	-36.868±58.997 cm/s
In-Track	-6390.592±2077.816 m	-343.420±61.316 cm/s
Cross-Track	-273.064±150.963 m	7.962±50.274 cm/s
3d-err	3976.106±3112.336 m	274.289±110.652 cm/s

Table 6.4: Hills Simulation with the zero measurements

6.4 Full Visibility

The aim of this section is to provide a baseline and to analyze the impact of the the bi-static measurements.

6.4.1 Signal Visibility

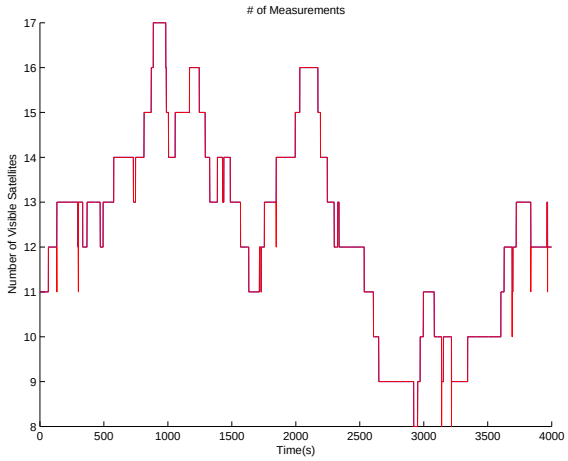

Figure 6.13: Full Visibility SV Plot: This plot shows the signal availibility as seen by the Shuttle during the Rendezvous. There over 8 satellites in view at all times, hence exceeding the minimum navigation requirement. In this scenario, any signal seen by the Hubble is assumed to provide a reflection.

6.4.2 High Fidelity Filter

The high fidelity model propagates both absolute states for the shuttle and the hubble. In the full visibility scenario, the little "blip" in the measurements is quite noticable. This is due to a mismatch in the drag models between my simulation and Hill's model. Since the size of the blip is quite large, it can likely be attributed to a parameter mismatch of some type.

6.4.2.1 Shuttle States

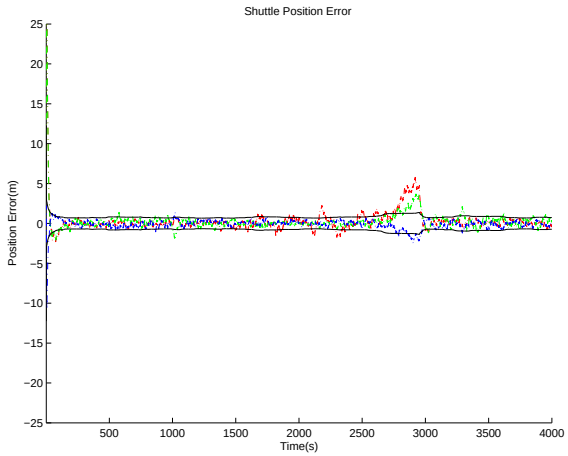

Figure 6.14: Full Visibility Shuttle Position Error: This plot shows the time evolution of the HST's velocity error in the ECI coordinate frame. The black lines represent the 3d-err covariance errors, while the red,green, and blue are the errors along I, J, and K vectors respectively. The 3d-err error is: 0.771 m mean and 0.548 m standard deviation.

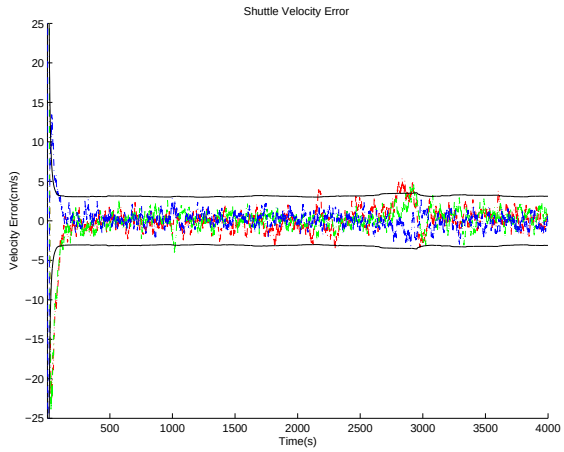

Figure 6.15: Full Visibility Shuttle Velocity Error: This plot shows the time evolution of the HST's velocity error in the ECI coordinate frame. The black lines represent the 3d-err covariance errors, while the red,green, and blue are the errors along I, J, and K vectors respectively. The 3d-err error is: 1.603 cm/s mean and 0.789 cm/s standard deviation.

6.4.2.2 Hubble States

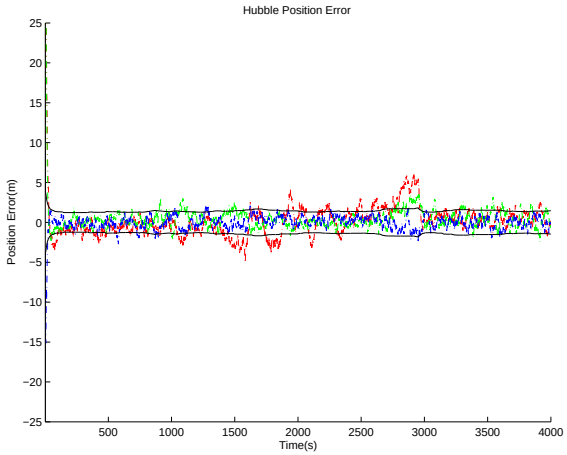

Figure 6.16: Full Visibility Hubble Position Error: This plot shows the time evolution of the HST's velocity error in the ECI coordinate frame. The black lines represent the 3d-err covariance errors, while the red,green, and blue are the errors along I, J, and K vectors respectively. The 3d-err error is: 1.427 m mean and 0.776 m standard deviation.

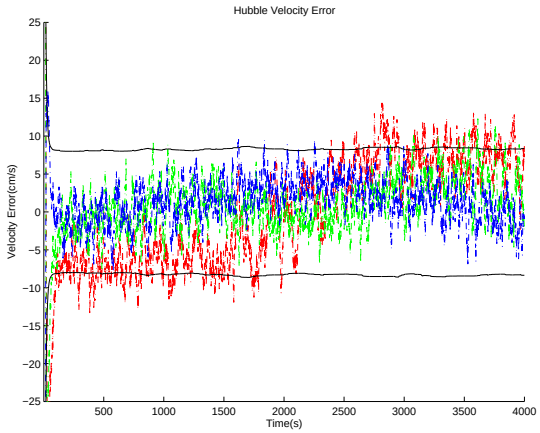

Figure 6.17: Full Visibility Hubble Velocity Error: This plot shows the time evolution of the HST's velocity error in the ECI coordinate frame. The black lines represent the 3d-err covariance errors, while the red,green, and blue are the errors along I, J, and K vectors respectively. The 3d-err error is: 5.39 cm/s mean and 2.408 cm/s standard deviation.

6.4.2.3 Optimal Reception

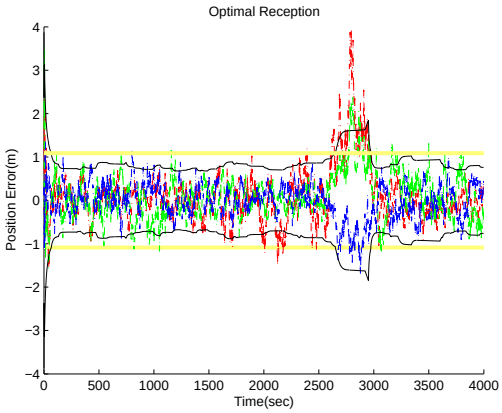

Figure 6.18: Full Visibility Optimal Relative Position: This plot shows the time evolution of the relative position error in the ECI coordinate frame. The black lines represent the 3d-err covariance errors, while the red,green, and blue are the errors along I, J, and K vectors respectively. The yellow line represents the best performance you can acheive, if Hubble was equipped with a tranceiver and a GPS receiver of its own. *This assumes no cross correlation of the measurements

6.4.2.4 Discussion

The receiver performs extremely well, with roughly $2m$ 3d-err standard deviation in the Shuttle's and HST's absolute Positions. If we pick an ideal case such that both are equipped with a tranceiver and GPS receiver, using their relative state information, and asumming no measurement correlation, then we can approximate the "optimal" position error as the yellow lines depicted in the previous figure. However, one of the benefits of using the differenced reflected signal, is that the bias and common mode errors difference out of the equation leaving us with a nearly pure measurement.

		Position $\mu \pm \sigma$	Velocity $\mu \pm \sigma$
Shuttle			
	$\hat{I}$	-0.198±0.678 m	0.126±1.136 cm/s
	$\hat{J}$	0.012±0.518 m	0.269±1.029 cm/s
	$\hat{K}$	0.035±0.356 m	-0.059±0.867 cm/s
	3d-err	0.771±0.548 m	1.603±0.789 cm/s
Hubble			
	$\hat{I}$	-0.554±0.866 m	-0.354±2.582 cm/s
	$\hat{J}$	0.467±0.918 m	2.909±3.765 cm/s
	$\hat{K}$	-0.103±0.714 m	-0.272±2.319 cm/s
	3d-err	1.427±0.776 m	5.392±2.408 cm/s

Table 6.5: High Fidelity Simulation with full signal avalibility

6.4.2.5 Configuration

For the full visibility scenario, the Kalman filter covariance matrices, P and Q were adjusted such that we would get the optimal performance from our filter. P was chosen to be $500 * \mathbf{I}_{13x13}$ for a reasonably fast convergence time, and the components of Q were chosen to be $\sigma_{ps}^2 = 1e-3$,$\sigma_b^2 = 5$ and $\sigma_{vs}^2 = 1e-3$ for the shuttle process noise. For the HST, the process noise components were chosen to be $\sigma_{ph}^2 = 1e-3$ and $\sigma_{vh}^2 = 1e-5$.

6.4.3 Hill's Filter

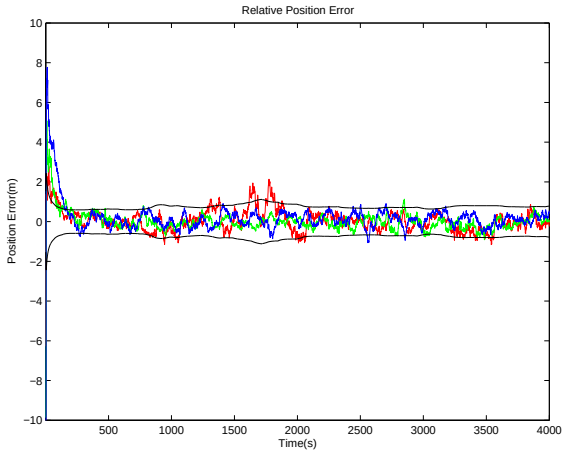

Figure 6.19: Full Visibility RIC Position Error: This plot shows the time evolution of the relative position error in the RIC coordinate frame. The black lines represent the 3d-err covariance errors, while the red,green, and blue are the errors along R, I, and C vectors respectively. The 3d-err error is: 0.562 m mean and 0.230 m standard deviation.

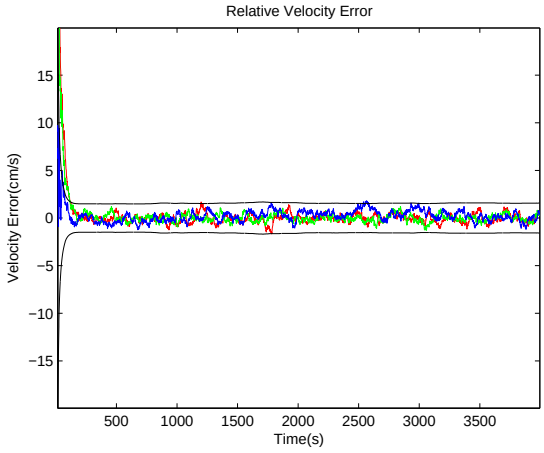

Figure 6.20: Full Visibility RIC Velocity Error: This plot shows the time evolution of the relative velocity error in the RIC coordinate frame. The black lines represent the 3d-err covariance errors, while the red,green, and blue are the errors along R, I, and C vectors respectively. The 3d-err error is: 0.73 cm/s mean and 0.293 cm/s standard deviation.

6.4.3.1 Discussion

Assuming that the reflected GPS measurements are readily availible, they provide a good position estimate. The position error is minimal, around $5m$. One of the convenient things about forming it purely in the relative frame is that a majority of the relative forces, biases, and errors difference out making this an ideal implementation.

	Position $\mu \pm \sigma$	Velocity $\mu \pm \sigma$
Radial	-0.102±0.382 m	-0.012±0.398 cm/s
In-Track	-0.083±0.309 m	-0.005±0.373 cm/s
Cross-Track	0.112±0.321 m	0.298±0.485 cm/s
3d-err	0.562±0.230 m	0.73± 0.293 cm/s

Table 6.6: Hills Simulation Full Visibility Error Table

For the full visibility scenario, the Kalman filter covariance matrices, P and Q were adjusted such that we would get the optimal performance from our filter. P was chosen to be $10 * \mathbf{I}_{6x6}$ for a reasonably fast convergence time, and the components of Q were chosen to be $\sigma_p^2 = 1e-4$ and $\sigma_v^2 = 1e-5$ for the relative process noise matrices, position and velocity respectively.

6.5 Increased Reflective Noise

The results presented in this section assume that all visible satellites in view are providing a reflected measurement. These are used to formulate the relative position. The noise variance was increased by a factor of 5 in this case, to demonstrate the effect of decreased reflective quality on the signal.

6.5.1 Signal Visibility

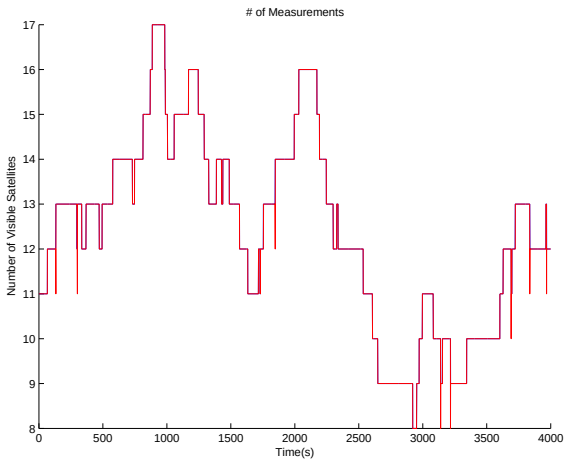

Figure 6.21: Increased Reflective Noise SV Plot: This plot shows the signal availibility. In this scenario we assume that all signals visible to the Hubble are producing reflected measurements

6.5.2 High Fidelity Filter

6.5.2.1 Shuttle States

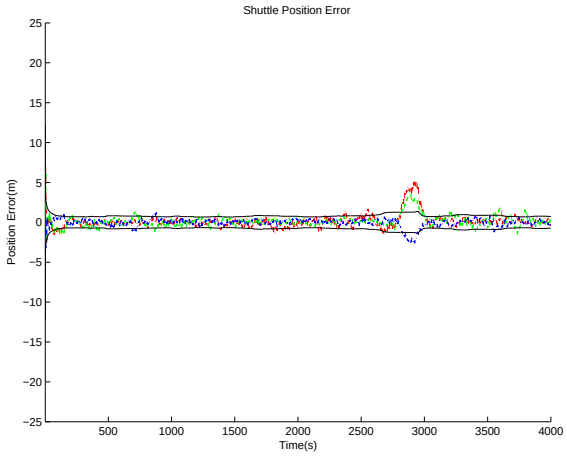

Figure 6.22: Increased Reflective Noise Shuttle Position Error: This plot shows the time evolution of the Shuttle's position error in the ECI coordinate frame. The black lines represent the 3d-err covariance errors, while the red,green, and blue are the errors along I, J, and K vectors respectively. The 3d-err error is: 1.019 m mean and 1.224 m standard deviation.

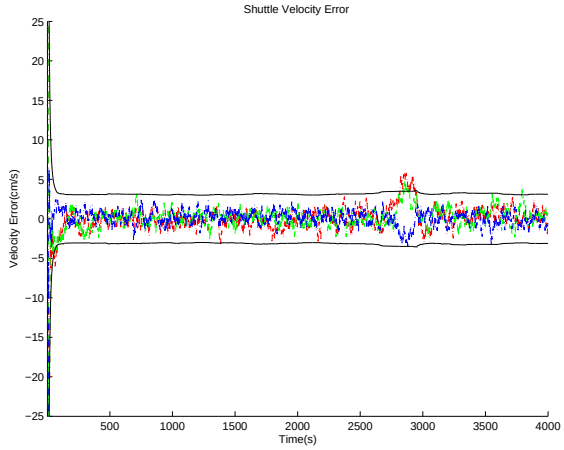

Figure 6.23: Increased Reflective Noise Shuttle Velocity Error: This plot shows the time evolution of the Shuttle's velocity error in the ECI coordinate frame. The black lines represent the 3d-err covariance errors, while the red,green, and blue are the errors along I, J, and K vectors respectively. The 3d-err error is: 1.864 cm/s mean and 1.275 cm/s standard deviation.

6.5.2.2 Hubble States

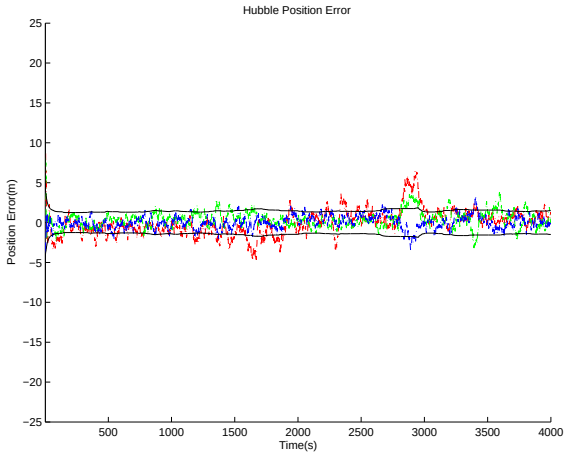

Figure 6.24: Increased Reflective Noise Hubble Position Error: This plot shows the time evolution of the HST's position error in the ECI coordinate frame. The black lines represent the 3d-err covariance errors, while the red,green, and blue are the errors along I, J, and K vectors respectively. The 3d-err error is: 1.834 m mean and 1.258 m standard deviation.

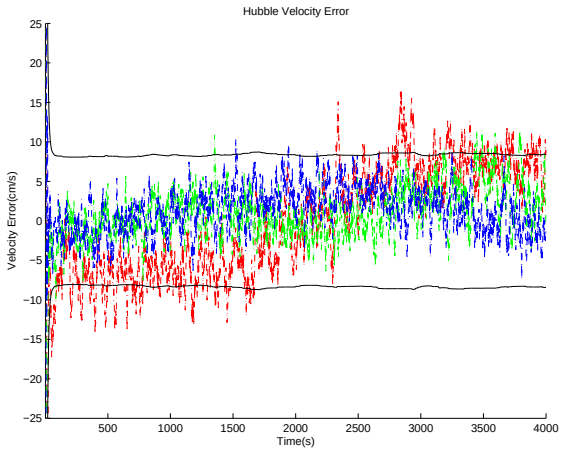

Figure 6.25: Increased Reflective Noise Hubble Velocity Error: This plot shows the time evolution of the HST's velocity error in the ECI coordinate frame. The black lines represent the 3d-err covariance errors, while the red,green, and blue are the errors along I, J, and K vectors respectively. The 3d-err error is: 8.151 cm/s mean and 2.720 cm/s standard deviation.

6.5.2.3 Discussion

The increased reflective noise in the system only increased the error of the filter a nominal amount. Although the error was increased by a factor of 5, it is barely noticable in the error states. The Kalman filter works by weighting spreading the error across the states. The weighting on the dynamic model likely helped filter off the increased noise, keeping the totals low. Since, the direct measurements are the same, heavier reliance on the Shuttle's position and the dynamic model of the hubble keep the errors down.

		Position $\mu \pm \sigma$	Velocity $\mu \pm \sigma$
Shuttle			
	$\hat{I}$	0.414±1.107 m	0.554±1.507 cm/s
	$\hat{J}$	0.313±0.818 m	0.375±1.216 cm/s
	$\hat{K}$	-0.138±0.595 m	-0.121±0.943 cm/s
	3d-pos err	1.019±1.224 m	1.864±1.275 cm/s
Hubble			
	$\hat{I}$	0.890±1.381 m	5.698±3.817 cm/s
	$\hat{J}$	0.418±1.120 m	2.009±3.340 cm/s
	$\hat{K}$	0.198±0.883 m	1.920±2.817 cm/s
	3d-pos err	1.834±1.258 m	8.151±2.720 cm/s

Table 6.7: High Fidelity Simulation with Increased Noise

6.5.2.4 Configuration

For the full visibility scenario, the Kalman filter covariance matrices, P and Q were adjusted such that we would get the optimal performance from our filter. P was chosen to be $500 * \mathbf{I}_{13x13}$ for a reasonably fast convergence time, and the components of Q were chosen to be $\sigma_{ps}^2 = \sigma_b^2 = 0.2$ and $\sigma_{vs}^2 = 0.1$ for the shuttle process noise. For the HST, the process noise components were chosen to be $\sigma_{ph}^2 = 0.2$ and $\sigma_{vh}^2 = 0.05$.

6.5.3 Hill's Filter

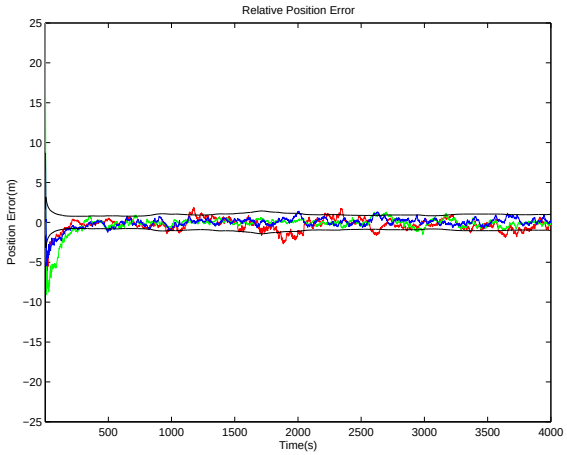

Figure 6.26: Increased Noise RIC Position Error: This plot shows the time evolution of the relative position error in the RIC coordinate frame. The black lines represent the 3d-err covariance errors, while the red,green, and blue are the errors along R, I, and C vectors respectively. The 3d-err error is: 0.850 m mean and 0.440 m standard deviation.

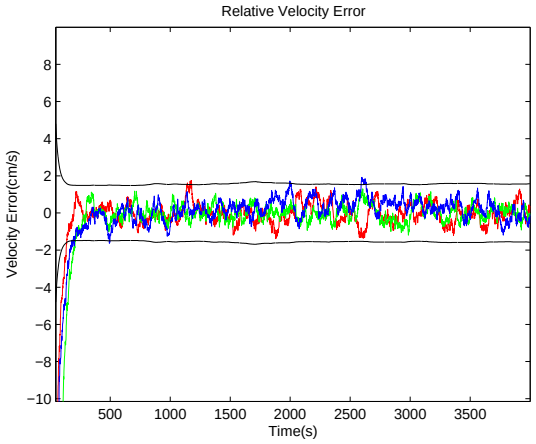

Figure 6.27: Increased Noise RIC Velocity Error: This plot shows the time evolution of the relative velocity error. The black lines represent the 3d-err covariance errors, while the red,green, and blue are the errors along R, I, and C vectors respectively. The 3d-err error is: 0.875 cm/s mean and 0.378 cm/s standard deviation.

6.5.3.1 Discussion

Similarly Hill's simulation encountered only a nominal increase in position error. This is likely caused by its reliance on purely the reflected measurements.

	Position $\mu \pm \sigma$	Velocity $\mu \pm \sigma$
Radial	-0.280±0.658 m	0.033±0.561 cm/s
In-Track	-0.056±0.475 m	-0.021±0.437 cm/s
Cross-Track	0.132±0.400 m	0.353±0.527 cm/s
3d-err	0.850±0.440 m	0.875±0.378 cm/s

Table 6.8: Hills Simulation with Increased Noise Error Table

For the increased noise scenario, the Kalman filter covariance matrices, P and Q were left the same, so that we would get a comparative performance from our filter, in the face of increased reflective noise. P was chosen to be $0.5 * \mathbf{I}_{6x6}$ for a reasonably fast convergence time, and the components of Q were chosen to be $\sigma_p^2 = 25$ and $\sigma_v^2 = 25$ for the relative process noise matrices, position and velocity respectively.

6.6 Adding the GPS Visibility Mask

This simulation is limited to the first 800 seconds. The actual "Docking" in the STK simulation is simply an uncontrolled collision which occurs roughly 800 seconds in. The visibility mask was generated from an actual docking scenario including thruster firings, and then mapped onto the first 800 seconds of this simulation. The

actual docking process plays a huge roll on reflected signal availibility and only an approximation can be made. The primary intention of this section is to demonstrate the inclusion of the reflected measurements as they become availible.

6.6.1 Signal Visibility

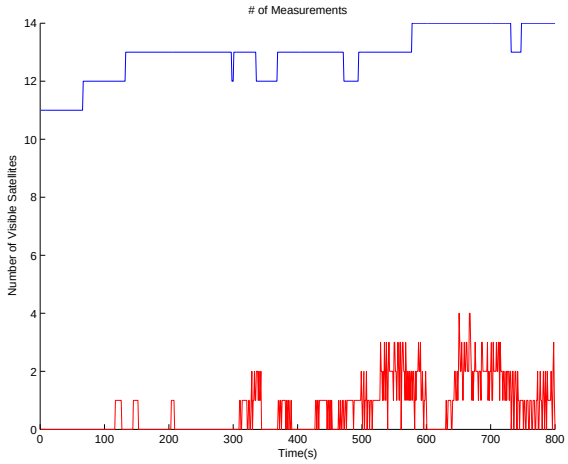

Figure 6.28: This plot shows the number of visible GPS signals availible(blue line) and the number of visible reflections(red line)

6.6.2 High Fidelity Filter

6.6.2.1 Shuttle States

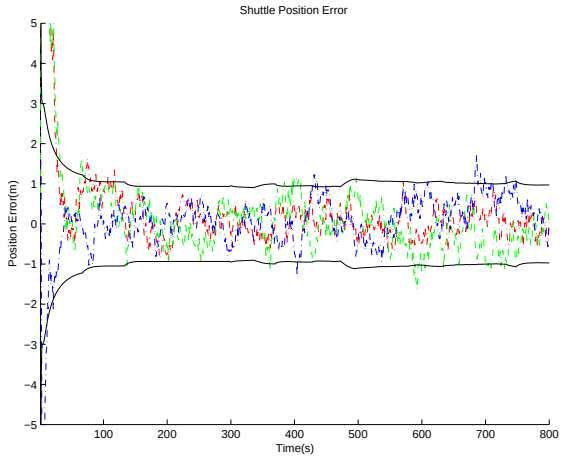

Figure 6.29: High Fidelity Simulation with Visibility Mask - Shuttle Position Error: This plot shows the time evolution of the Shuttle's position error in the ECI coordinate frame. The black lines represent the 3d-err covariance errors, while the red,green, and blue are the errors along I, J, and K vectors respectively. The 3d-err error is: 2.03 m mean and 1.25 m standard deviation.

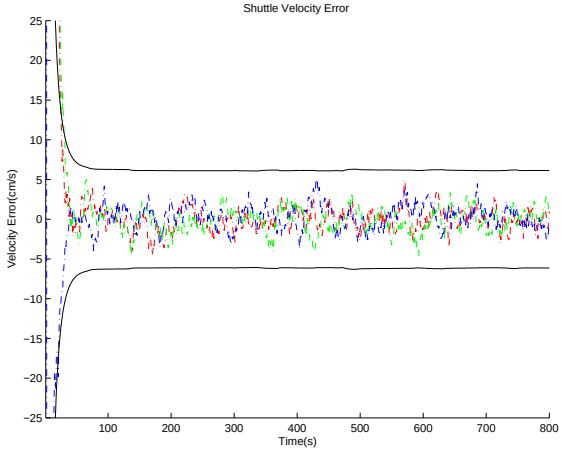

Figure 6.30: High Fidelity Simulation with Visibility Mask - Shuttle Velocity Error: This plot shows the time evolution of the Shuttle's velocity error in the ECI coordinate frame. The black lines represent the 3d-err covariance errors, while the red,green, and blue are the errors along I, J, and K vectors respectively. The 3d-err error is: 21.0 cm/s mean and 9.9 cm/s standard deviation.

6.6.2.2 Hubble States

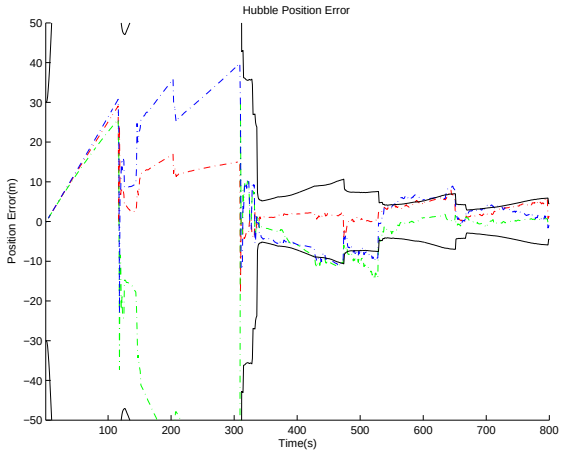

Figure 6.31: High Fidelity Simulation with Visibility Mask - Hubble Position Error: This plot shows the time evolution of the HST's position error in the ECI coordinate frame. The black lines represent the 3d-err covariance errors, while the red,green, and blue are the errors along I, J, and K vectors respectively. The 3d-err error is: 83.6 m mean and 49.1 m standard deviation.

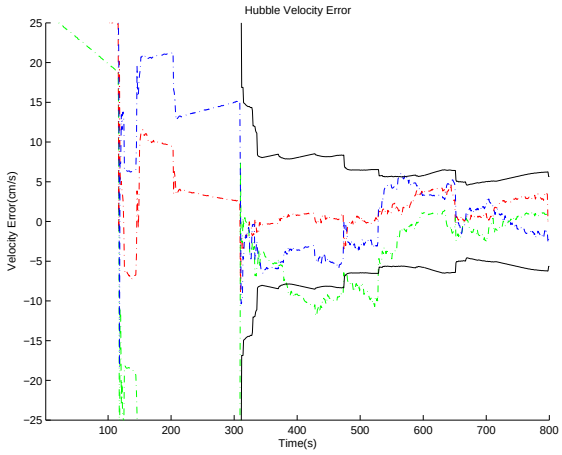

Figure 6.32: High Fidelity Simulation with Visibility Mask - Hubble Velocity Error: This plot shows the time evolution of the HST's velocity error in the ECI coordinate frame. The black lines represent the 3d-err covariance errors, while the red,green, and blue are the errors along I, J, and K vectors respectively. The 3d-err error is: 111 cm/s mean and 44.9 cm/s standard deviation.

6.6.2.3 Discussion

The shuttle's position is well known throughout the simulation. The initial Hubble states begin to diverge until the first of the measurements are encountered. These measurements serve to pull the estimates closer to their truth values.

		Position $\mu \pm \sigma$	Velocity $\mu \pm \sigma$
Shuttle			
	$\hat{I}$	0.029±0.767 m	-0.155±11.034 cm/s
	$\hat{J}$	-0.019±1.735 m	1.035±14.992 cm/s
	$\hat{K}$	0.024±1.452 m	-2.243±13.701 cm/s
	3d-err	2.031±1.254 m	20.999±9.913 cm/s
Hubble			
	$\hat{I}$	-11.658±54.743 m	14.032±78.765 cm/s
	$\hat{J}$	-36.552±36.969 m	-23.729±58.672 cm/s
	$\hat{K}$	-25.304±54.306 m	16.088±62.171 cm/s
	3d-err	83.656±49.136 m	111.724±44.936 cm/s

Table 6.9: High Fidelity Simulation - Using the SV Visibility Mask

6.6.2.4 Configuration

For the full visibility scenario, the Kalman filter covariance matrices, P and Q were kept the same as in the full visibility scenario. P was chosen to be $500 * \mathbf{I}_{13x13}$ for a reasonably fast convergence time, and the components of Q were chosen to be

$\sigma_{ps}^2 = 1e-3$,$\sigma_b^2 = 5$ and $\sigma_{vs}^2 = 1e-5$ for the shuttle process noise. For the HST, the process noise components were chosen to be $\sigma_{ph}^2 = 1e-2$ and $\sigma_{vh}^2 = 1e-3$.

6.6.3 Hill's Filter

The initial relative states begin to diverge until the first of the measurements are encountered. The first measurement yanks the estimate away from the truth values. This is likely due to a poor geometry with respect to one measurement. As more satellites become availible the position error begins to converge again.

6.6.3.1 Relative States

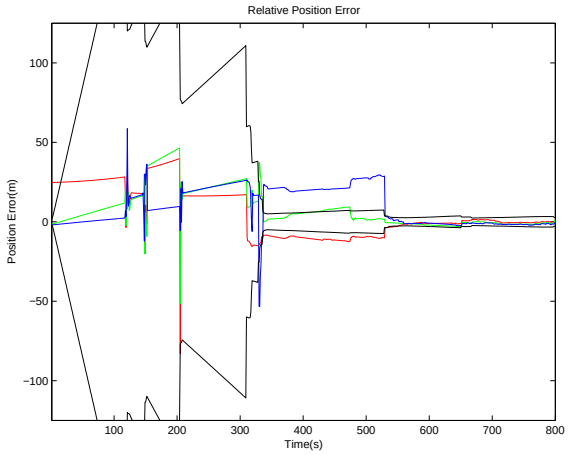

Figure 6.33: Visibility Mask RIC Position Error: This plot shows the time evolution of the relative position error. The black lines represent the 3d-err covariance errors, while the red,green, and blue are the errors along R, I, and C vectors respectively. The 3d-err error is: 97.14 m mean and 56.5 m standard deviation.

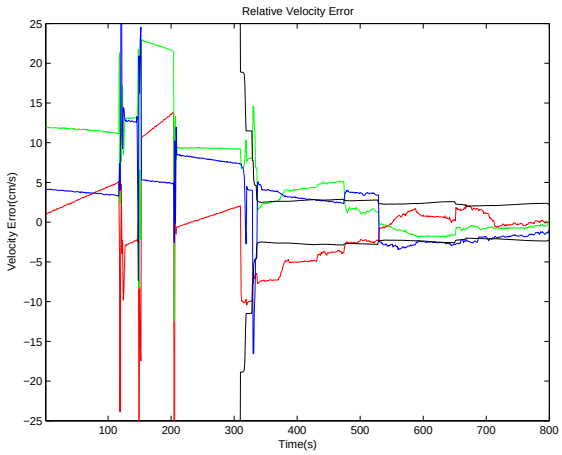

Figure 6.34: Visibility Mask RIC Velocity Error: This plot shows the time evolution of the relative velocity error. The black lines represent the 3d-err covariance errors, while the red,green, and blue are the errors along R, I, and C vectors respectively. The 3d-err error is: 64.0 cm/s mean and 36.9 cm/s standard deviation.

	Position $\mu \pm \sigma$	Velocity $\mu \pm \sigma$
Radial	12.783±28.107 m	4.595±18.560 cm/s
In-Track	-16.530±23.812 m	-10.686±20.922 cm/s
Cross-Track	-40.420±46.550 m	2.046±22.105 cm/s
3d-err	97.631±56.453 m	64.052±36.945 cm/s

Table 6.10: Hills Simulation Visibility Mask Error Table

For the Hill's scenario, the Kalman filter covariance matrices, P and Q were kept as the same as in the full visibility case. P was chosen to be $0.5 * \mathbf{I}_{6x6}$ for a reasonably fast convergence time, and the components of Q were chosen to be $\sigma_p^2 = 1e-3$ and $\sigma_v^2 = 1e-5$ for the relative process noise matrices, position and velocity respectively.

Chapter 7

Conclusion

7.1 Concluding Remarks

Bi-static radar in general can be a useful tool for rendezvous and docking scenarios. While it is not the best solution since LIDAR and RADAR can provide far better ranging accuracies. LIDAR and RADAR are sub-mm accuracies, while the Bi-static GPS based radar is sub cm. The GPS reflections itself is by nature, jamming resistant(from the signal structure), passive, and does not require additional hardware. Again, since there is no good experimental data of tracking a GPS reflection in real time and solving for a relative solution, it is impossible to accurately quantify performance results until some representative test data has been collected from HST-SM4. Since almost all of LEO, GEO and parts of HEO are bathed in GPS radiation, it makes sense to attempt to harness this free source of energy to provide an extra measurement for the Kalman filter. It comes complete with an accurate baseline and pseudorange code to lock on to. Thus enabling docking with a dead satellites, requiring less power, less instrumentation, and less mass. The only added cost is algorithmic complexity for the radar analysis, and the question of testing the system.

7.1.1 GPS as a Bi-Radar Measurement

Radar is a very important tool for relative navigation in space. Adding an additional measurement such as a bi-static range measurement could improve, or aid an OD filter. However, GPS based bi-static radar is not without its drawbacks. The bi-static radar scenario for relative navigation is extremely sensitive to the geometry of the problem. In this particular analysis, the Shuttle is essentially approaching from below and facing the GPS constellation. Effectively placing all of the satellites within the bi-static cross section region, reducing visibility. Very few, if any satellites cross into the fringes of the pseudo-monostatic radar cross section and forward scattering regions. This makes this particular truth model very sensitive to not only the attitude of Hubble and the Shuttle, but also the time, day and orientation of the GPS constellation. All of these factors change rapidly and would require extensive analysis to determine reflective visibility. Moreover, any slight miscalculation, could result in a sharp drop in signal strength due to the sharp drop off in signal power from the sinc and bessel functions making it almost impossible to detect a single satellite.

One possible remedy to solving the visibility problem, would be an approach from the side with an LHCP antenna's back to the constellation and facing the target. It would also have an additional RHCP antenna directly facing the constellation. This would force the bi-static angle to be small, and force reflections into the pseudo-monostatic region. This would greatly increase the visibility of reflections.

While using reflected GPS signals may not be the best solution for relative

navigation. It has the possibility to provide an extra measurement and offer some level of redundancy for the system. Some of the major drawbacks is of using the bi-static radar approach are the visibility of the signal, the powerlevel of the reflections, and the geometry with respect to the GPS constellation. The primary advantage of this system is that with an extra antenna, and some added algorithmic complexity, it is possible to determine a relative position.

7.1.2 Orbit Filters

The orbit filters work wonderfully when supplied with a decent initialization and an accurate absolute position estimate of the Shuttle. Even without a reflection, a good dynamic model, can carry the estimates along a close trajectory. When measurements come online, they help minimize the error covariance. This is particularly important when conducting maneuvers and adding any other uncertainties or forces not incorporated in the dynamic model.

7.1.3 Model Comparison

Hill's filter actually performed better than the high fidelity model. This is likely due to the model mismatch between the truth plant and my estimated drag model. Since the relative forces are small in hill's frame, the relative error did not grow. In the high fidelity model, the drag perturbations were cumulative adding up the error as it propagated forward.

In the situation with increased noise, there is very little perturbation to the

errors in both models. This is due to a heavy weighting in the process noise matrix, effectively usign the dynamics to propagate as opposed to relying on noiser measurements. If the High fidelity model's drag term is corrected, it will likely out-perform Hill's model.

7.1.4 Practical Considerations

In order to realistically implement either Hill's model or the high fidelity model, a GPS receiver with sufficient processing power is needed. Hill's model requires two rotations, each visible GPS satellite producing a reflection must first be propagated from ECEF to ECI, then again to Hill's frame. This requires many matrix multiplications. Hill's model also has 6 states, each of whcih needs to be propagated. This can amount to a large processing burden, especially if the flight card does not have a floating point unit. Hill's filter does require the shuttle's position as an input. This can come from either another filter another instrument.

The high fidelity model is not a good candidate for real time implementation. It requires 13 states, and each GPS satellite must be converted from ECEF to ECI in order to perform a navigation solution. In addition to the extra states, hence larger Q matrix, it also requires that Φ and the states be propagated in an ODE solver. This is burdensome, even for a current desktop computer as of 2007.

In the future, I plan to implement Hill's filter on the Navigator GPS receiver. This features a 65.536 Mhz processor, and it also has a double precision multiply on one of the field programmable logic gate array(FPGA).

7.2 Future Work

One area for future work would be to use numeric methods to solve the reflection equations. This would provide a better model for the reflective properties, and help deduce the received signal power and the variance in the pseudorange measurements. In addition to advanced reflection modeling, some empirical data can be recorded using an anechoic chamber and reflecting L band signals off of a cylinder of comparable size.

Another addition to the dynamic model would include a more accurate clock filter. Most GPS receivers include a form of clock drif, however, in order to simplify the relative equations only the first term, the bias was included.

Another area for future work is to improve upon the dynamic model. Other additions can include thruster firing and closed-loop feedback to actually implement a rendezvous maneuver. These models are also general enough to be applied to nearly any LEO rendezvous, particularly the high-fidelity model can be applied to nearly any orbit. An example for this could be use on MMS, formation flying mission in a highly elliptical orbit. While they are out of contact from GPS at apogee, they are well within the constellation, and even pass through the constellation at points in their orbits, providing for many opportunities for reflected measurements.

Over the next decade, a new set of GPS Satellites will be launched, each transmitting a modernized version of the GPS Signal; L2c and L5. These signals provide better coverage, improved signal strength, as well as a data-less code. The data-less code will allow for longer integration periods and improved measurements.

These could be incorporated into the pseudorange measurements, in addition to using a technique called "wide-laning" in order to determine the ionospheric bias directly.

When Navigator returns from the Hubble Servicing mission, the MSM will have recorded raw RF data for analysis. The raw data can be analyzed to determine the real received signal powers, visible satellites, and provide a radar cross section for the HST at L1. This will lay the framework for potential future unmanned missions to the HST, such as the deorbit module, when HST is scheduled to be dropped into the ocean.

Chapter A

Derivations

A.1 Hill's Equations of Motion

The equation of motion for the target craft is given by:

$$\ddot{r_t} = -\frac{\mu}{|r|_t^2}\hat{r_t} \tag{A.1}$$

The equation of motion for the interceptor craft is given by:

$$\ddot{r_i} = -\frac{\mu}{|r|_i^2}\hat{r_i} + \mathbf{F}_{thrust} \tag{A.2}$$

Now, defining the relative vector to the spacecraft, $r_r = r_i - r_t$, this gives us the relative equation of motion.

$$\ddot{r_r} = -\frac{\mu}{|r|_i^3}\hat{r_i} + \mathbf{F}_{thrust} + \frac{\mu}{|r|_t^3}\hat{r_t} \tag{A.3}$$

Now, to find the equation of motion for the interceptor, we solve for $r_i = r_t + r_r$.

The radius is give by $r_i = \sqrt{|r_t|^2 + 2|r_t||r_r| + |r_r|^2}$

Now

$$\frac{r_r}{|r_i|^3} = \frac{\vec{r_t} + \vec{r_r}}{(|r_t|^2 + 2|r_t||r_r| + |r_r|^2)^{\frac{3}{2}}} \tag{A.4}$$

Making the assumption that r_r is small compared to r_t and r_r gives the relation

$$\frac{r_r}{|r_i|^3} = \frac{\vec{r_t} + \vec{r_r}}{|r_t|^3}\left(1 + \frac{2r_t \cdot r_r}{|r_t|^2}\right)^{\frac{-3}{2}} \tag{A.5}$$

Now using the binomial series: $(1+x)^n = 1 + nx + \frac{n(n-1)x^2}{2!} + ..$ to expand the denomonator $\left(1 + \frac{2r_t \cdot r_r}{|r_t|^2}\right)^{\frac{-3}{2}}$

Now, substituting this equation into the original relative motion ODE, we get

$$\ddot{r}_r = -\mu \left(\frac{r_t + r_r}{r_t^3} \left(1 - \frac{3}{2} left \frac{2r_t \cdot r_r}{r_t^2} + ... \right) \right) + F_t hrust + \frac{\mu r_t}{r_t^3} \tag{A.6}$$

Now, cancelling terms and taking only a linear approximation we arrive at:

$$\ddot{r}_r = -\frac{\mu}{r_t^3} \left(-\frac{3r_t}{2} \left(\frac{2r_r \cdot r_r}{r_t^2} \right) + r_r - \frac{3r_r}{2} \left(\frac{2r_r \cdot r_r}{r_t^2} \right) \right) + \vec{F}_t hrust \tag{A.7}$$

Now assuming that $\left(\frac{2r_r \cdot r_r}{r_t^2}\right)$ is small compared to the actual range, we can drop this term. Giving us now:

$$\ddot{r}_r = -\frac{\mu}{r_t^3} \left(-\frac{3r_t}{2r_t} \left(\frac{2r_r \cdot r_r}{r_t} \right) + r_r \right) + \vec{F}_t hrust \tag{A.8}$$

Now, we have $\hat{R} = \frac{2r_r \cdot r_r}{r_t}$ which is the direction of acceleration of the interceptor in the target frame. This reduces the equation to simply:

$$\ddot{r}_r = -\frac{\mu}{r_t^3} \left(-3x\hat{R} + r_r \right) + \vec{F}_t hrust \tag{A.9}$$

Now, solving for the relative acceleration in a rotating frame we use the equation[21].

$$\ddot{r}_i = \ddot{r}_r + \dot{\omega}_r \times r_r + 2\omega_r \times \dot{r}_r + \omega_r \times (\omega_r \times r_r) \tag{A.10}$$

Solving for the relative acceleration gives us:

$$\ddot{r}_r = \ddot{r}_i - \dot{\omega}_r \times r_r - 2\omega_r \times \dot{r}_r - \omega_r \times (\omega_r \times r_r) \tag{A.11}$$

Finally we arrive at the Clohessy-Wiltshire, or Hill's equations

$$\ddot{x} - 2\omega\dot{y} - 3\omega^2 x + fx = 0 \tag{A.12}$$

$$\ddot{y} + 2\omega\dot{x} + fy = 0 \tag{A.13}$$

$$\ddot{z} + \omega^2 z + fz = 0 \tag{A.14}$$

or, by defining $\vec{x}^T = (\vec{x}, \dot{\vec{x}})$, then we get the form

$$\dot{\vec{x}} = \begin{bmatrix} 0 & 0 & 0 & 1 & 0 & 0 \\ 0 & 0 & 0 & 0 & 1 & 0 \\ 0 & 0 & 0 & 0 & 0 & 1 \\ 3\omega^2 & 0 & 0 & 0 & 2\omega & 0 \\ 0 & 0 & 0 & -2\omega & 0 & 0 \\ 0 & 0 & \omega^2 & 1 & 0 & 0 \end{bmatrix} \vec{x} + \begin{bmatrix} 0 & 0 & 0 \\ 0 & 0 & 0 \\ 0 & 0 & 0 \\ 1 & 0 & 0 \\ 0 & 1 & 0 \\ 0 & 0 & 1 \end{bmatrix} \vec{u} \tag{A.15}$$

Bibliography

[1] W. Bamford ,*Naviation and Control of Large Satellite Formations*,Ph.D. Disseration, The Univeristy of Texas at Austin, TX,December 2004.

[2] E. Knott , *Radar Handbook* McGraw Hill, New York, NY, 2nd ed.,Chap. 11, 2001.

[3] R. G. Brown, *Introduction to Random Signal Analysis and Kalman Filtering* John Wiley & Sons Inc., New York, NY, Chap. 7-8. 2nd ed., 1983.

[4] D. Gaylor, G. Lightsey, ,"Effects of Multipath and Signal Blockage on GPS Navigation in the Vicinity of the International Space Station(ISS)",*AIAA Guidance, Navigation, and Control Conference and Exhibit*,Austin, TX, August 11-14, 2003.

[5] D. Gaylor, G. Lightsey, K. Key ,"GPS/INS Kalman Filter Design for Spacecraft Operating in the Proximity of the International Space Station",*AIAA Guidance, Navigation, and Control Conference and Exhibit*, Austin, TX,August 11-14, 2003.

[6] Y.S. Hsu, D.C. Lorti, "Spaceborne Bistatic Radar - An Overview",*IEE Proceedings*, Vol. 133, Pt. F, No. 7, pp. 642-648, 1986.

[7] Johnson, A.E., et al, "Lidar-Based Hazard Avoidance for Safe Landing on Mars". *Journal of Guidance, Control, and Dynamics*, Vol. 25, no. 6, pp. 1091-1099, 2002.

[8] L. Iorio, "The impact of the static part of the Earth's gravity field on some tests of general relativity with satellite laser ranging". *Celestial Mechanics & Dynamical Astronomy,*, Vol. 86, pp. 277-294, 2003.

[9] D. Manandhar, R. Shibasaki, "GPS Signal Anaylsis using LHCP/RHCP Antenna and Software",*ION GNSS 17th International Technical Meeting of the Satellite Division*,Long Beach, CA. pg. 2489 Sept 21-24, 2004.

[10] D. Masters, et al.,"A Passive GPS Bistatic Radar Altimeter for Aircraft Navigation",*ION GPS 2001*, Salt Lake City, UT, 2001.

[11] D. Masters,V. Zavorotny,S. Katzberg,W. Emery, "GPS Signal Scattering from Land for Moisture Content Determination",*International Geoscience and Remote Sensing Symposium*, July 24-28, 2000.

[12] ARINC Research Corp *NavStar GPS SpaceSegment / Navigation User Interfaces*, El Segundo, CA ,October 10, 2003.

[13] NASA ,*Space Shuttle News Reference*, US Government Printing Office,1981.

[14] E. Kaplan ,*Understanding GPS Principals and Applications*, Artech House Publishers, Norwood MA, 1996.

[15] A, Moccia, et al. "Performance of spaceborne bistatic synthetic aperture radar". *IEEE Transactions on Aerospace and Electronic Systems*, Volume 41, Issue 4,pp 1383-1395, Oct. 2005,

[16] HubbleSite, http://hubblesite.org/reference_desk/facts_.and._figures/quick_facts/, retrieved 3/09/2007

[17] B. W. Parkinson, J.J Spilker *Global Positioning System: Theory and Applications*, Vol. 1 American Institute of Aeronautics and Astronautics, Washington, DC, 1996.

[18] B. W. Parkinson, J.J Spilker *Global Positioning System: Theory and Applications*,Vol. 2, American Institute of Aeronautics and Astronautics, Washington, DC, 1996.

[19] Sensor Systems Inc. *GPS S67-1575 Series*, Chatsworth, CA 91311

[20] M. Skolnik, *Radar Handbook* McGraw Hill,2nd ed. Chap. 1-5, New York, NY, 2001.

[21] D.A. Vallado, *Fundamentals of Astrodynamics and Applications* McGraw Hill, Chap. 1-5, New York, NY, 2001.

[22] J. Willis, *Radar Handbook* McGraw Hill, New York, NY, Chap. 25. 2nd ed, 2001.